Multi-color photographic surface photometry of the Andromeda galaxy

Walterbos, R.A.M.; Kennicutt jr., R.C.

ASTRONOMY & ASTROPHYSICS
SUPPLEMENT SERIES

MAY 1987, PAGE 311

Astron. Astrophys. Suppl. Ser. **69,** 311-332 (1987)

Multi-color photographic surface photometry of the Andromeda galaxy

R. A. M. Walterbos ([1,*]) and R. C. Kennicutt, Jr. ([2])

([1]) Leiden Observatory, P.O. Box 9513, NL-2300 RA Leiden, The Netherlands
([2]) University of Minnesota, Department of Astronomy, 116 Church Street S.E., Minneapolis, MN 55455, U.S.A.

Received November 6, accepted December 18, 1986

Summary. — We present full two-dimensional photographic photometry of the nearby spiral galaxy M31 in various colors. Calibrated plates in *U, B, V,* and *R* were obtained with the Burrell Schmidt telescope on Kitt Peak, together with some low noise IIIaJ and IIIaF exposures. The plates were digitized with the Astroscan reticon densitometer at a resolution of 8″ to 16″, corresponding to a linear resolution of 25 to 50 pc. We describe the reduction and calibration of the data, as well as a method used to remove the thousands of foreground stars that contaminate the image of the galaxy. Extensive comparisons of our data with published photometric scans show that the blue light intensity of the galaxy is reliably measured out to about 20 kpc radius. Color maps with a typical uncertainty between 0.1 and 0.2 mag were obtained over the main part of the bulge and disk out to 14 kpc radius. Tables listing the intensity and color profiles along the principal axes of the galaxy are presented, together with global profiles in *U, B, V,* and *R* out to 24 kpc radius, obtained by integrating the intensity distributions in ellipses. Two-dimensional color maps, smoothed to a resolution of 40″, show the major dust lanes and a relatively bluer color in the ring of Population I material around 10 kpc radius. The colors continue to get bluer for larger radii. The colors of the bulge and disk inside the 10-kpc ring are fairly constant with *B-V* of 0.9 to 1.0 and *U-B* between 0.45 and 0.55. These are the colors characteristic of an old stellar population. A deep image obtained from the IIIaJ plates confirms earlier evidence for a warping of the stellar disk at a distance of 20 kpc from the centre. The isophotes of the dwarf elliptical companion NGC 205 are strongly twisted, suggesting tidal interaction between the elliptical and M31.

Key words : galaxies : M31 — spiral — structure of — stellar content of — photometry — image processing.

1. Introduction.

The Andromeda galaxy, at a distance of 690 kpc (Baade and Swope, 1963) the closest large spiral galaxy, is a key object for the study of the structure and the evolution of galaxies. The high spatial resolution that can be obtained (1′ corresponds to 200 pc) is particularly important for radio and infrared observations. The radio continuum emission from M31 has been mapped at high resolution (0.5 to 2.5) with the Effelsberg and Westerbork radio telescopes (Berkhuijsen *et al.,* 1983 ; Bystedt *et al.,* 1984 ; Walterbos *et al.,* 1985). High resolution data on the atomic hydrogen distribution are available from recent surveys made with the Cambridge telescope (Unwin, 1980a, 1980b) and with the Westerbork telescope (Brinks and Shane, 1984). The Infrared Astronomical Satellite has produced unique maps of the infrared emission from the dust (Habing *et al.,* 1984 ; Walterbos and Schwering, 1987). In addition, several regions in M31 have been observed in emission lines of CO in order to trace the distribution of molecular hydrogen (e.g. Stark, 1985 ; Ryden and Stark, 1986). In contrast to this wealth of new radio and infrared material on the gas and dust, relatively little quantitative information is available on the global properties of the stellar component. The main reason for this is that the large angular size of the galaxy aggravates the difficulties inherent in accurate optical multi-color surface photometry ; only with modern plate scanning devices and large computers has such work become possible. Hodge and Kennicutt (1982)

Data obtained at Kitt Peak National Observatory, (National Optical Astronomy Observatories, which is operated by the Association of Universities for Research in Astronomy, Inc., under contract with the National Science Foundation). Observations made with the Burrell Schmidt telescope of the Warner and Swasey Observatories, Case Western Reserve University.

(*) Present address : The Institute for Advanced Study, School of Natural Sciences, Princeton, NJ 08540, U.S.A.

Send offprint requests to : R. Walterbos.

obtained two-dimensional photographic photometry of the whole galaxy in one color band (*B*). To extend their work and to complement the data on the gas and dust we have obtained full two-dimensional photographic photometry of M31 in four broad-band colors (*U, B, V* and *R*) at moderate resolution (8″ to 16″). These data have been used to study the structure of the bulge, disk, and spiral arms, the distribution of stellar colors across the disk, and the extinction in the dust lanes. In this paper we will present the new optical data with only a brief discussion of some results ; subsequent papers will deal with the analysis of the material and discuss the correlations between the gas and the dust as derived from the radio and optical surveys. A subsequent paper will also describe narrow-band Hα photometry which we have measured in order to derive the absolute luminosities of the HII regions.

Surface photometry of a galaxy as big as M31 presents problems, not usually encountered with other galaxies. Even with a Schmidt telescope, the galaxy barely fits on one plate. Several instrumental and intrinsic effects on the sky background, which form the major limitations to all photometry at low light levels, have to be considered. Over the area necessary to cover M31, photographic plates in general will not be uniform. In addition, vignetting and light scattering in the telescope may be important. Intrinsic sky variations to be expected include a gradient in sky background due to the Milky Way (M31 is at a galactic latitude of $-21°$) as well as local night-sky brightness variations (depending on zenith angle and hour angle during exposure). Another problem is presented by the large number of foreground stars. Photoelectric drift scans do not suffer as much from instrumental variations that influence the background, but they have limited spatial coverage, coarse resolution, and low signal-to-noise ratio at faint light levels. Much photoelectric work has been done, however, and much of what is known so far about the colors of the galaxy comes from that work (cf. Sect. 4.1).

With modern digitization and analysis techniques several of the problems with photographic plates can be quantitatively assessed and, to a certain extent, solved. Furthermore, the large amount of published photoelectric and other single-scan data, provides a valuable check on the calibration of the photographic photometry and can be used to set the absolute zero level. The following steps were involved in the reduction of our material :

(1) Digitization of plates (Sect. 2).

(2) Compression of digitized images to low resolution maps, corrected for the presence of foreground stars. The low resolution maps were used to assess sky variations and make fits to the sky background (Sect. 3.1 and 3.2).

(3) Conversion of densities to intensities and subtraction of sky background (Sect. 3.3).

(4) Separation of plates of good and poor quality based on image and photometric quality, and combination of long and short exposures (Sect. 3.4).

(5) Removal of foreground stars (Sect. 3.5).

(6) Absolute calibration and evaluation of the accuracy of our photometry based on plate/plate comparisons and on comparisons with published data (Sect. 4).

Some results in the form of profiles along the main axes and color maps are presented in section 5.

2. Plate material and reduction.

The plates were taken with the F3.5 Burrell Schmidt telescope on Kitt Peak, which has a 61-cm correction plate and a 94-cm mirror. The correction plate is made from Schott UBK7 glass and consequently has good transmission in the ultraviolet. The plate scale is $96\farcs6\ \mathrm{mm}^{-1}$. The plate dimensions are about $20 \times 20\ \mathrm{cm}^2$, giving a field size of 5.16×5.16 degrees^2. The rather coarse plate scale is well suited to our project (and in fact dictated the choice of telescope) and keeps the area that has to be scanned within an acceptable range.

The emulsion and filter combinations were chosen to match closely the Johnson *UBV* system, to facilitate comparison of our data with theoretical calculations of colors of evolving stellar populations, and to enable absolute calibration by comparison with published photoelectric data. Exposures in a photographic *R* band were also obtained (note that this is *not* the Johnson *R* band). Our emulsion and filter combinations are the same as those used by Talbot *et al.* (1979) in their extensive study of M83. The transformations to the Johnson *UBVR* system are given by Jensen *et al.* (1981). For the *U, B,* and *V* bands the corrections are small : $\leqslant \pm 0.04$ mag over the range of interest. We also took some exposures on IIIaJ and IIIaF emulsions, that have low plate noise and are useful for studying the structure of the galaxy. We will refer to these as J and F exposures (the designation « J » should not be confused with the *infrared J* band). Van der Kruit and Searle (1981) give the transformations between the J and F bands and the Johnson *UBV* colors. The IIIa plates have calibration curves different from those of the other material and thus provide an additional check on our calibration. A log of the observational material is given in table I. We also made some short exposures so that a wide range in intensity could be covered. The *U* plates were not saturated in the centre and short exposures in *U* were not necessary. All plates were baked for the prescribed time in forming gas (2 % H_2, 98 % N_2) and developed in D-19 in a rocking tray. Immediately after the exposure in the telescope, sensitometer spots with different exposure times were projected onto the plates with the same filter in the light path as that in the telescope. For roughly half of the plates two sets of spots with different exposure

times were projected onto two corners, in order to obtain more points for the definition of the characteristic curve, and to check the calibration of the Kitt Peak sensitometer.

The plates were scanned in Leiden on the Astroscan device, a multi-element microdensitometer which employs a reticon of 128 diodes. In one scan the 128 diodes cover a strip of 1280 μm wide on the plate. A description of the instrument and its calibration is given by Swaans (1981). The transmission through 10×10 μm^2 pixels is recorded and automatically converted to density. The area that was scanned on each plate is shown in figure 1. Before digitizing the galaxy the plates were positioned on the Astroscan by measuring faint standard stars ; this could be done to within 10 μm accuracy so that interpolations were not necessary for obtaining color images. (Differences in plate scale due to temperature and color effects are more severe, though still only 40 to 80 μm across the full length of a plate). The major axis of the galaxy was placed parallel to the scan direction, assuming a position angle of exactly 38°. To keep the amount of data within acceptable limits and to improve the signal-to-noise ratio, the pixel size was on-line reduced to 40×40 μm^2 (3.″864 × 3.″864) by averaging the densities of 4×4 pixels. The galaxy was digitized in several fields (Fig. 1). Even with the reduced pixel size, more than 2000×4000 data points were recorded per plate.

The maximum density that can be measured by the Astroscan is limited by the intensity of the illuminating lamp. At maximum lamp intensity, the read-out noise dominates the plate noise at $D > 3.5$ (depending on emulsion type). By averaging several transmission measurements before conversion to density, the maximum density that can be reliably measured is increased to $D = 4.5$. Small fields centred on the bulge of M31 and on the two elliptical companions were therefore digitized with a very high repetition factor (32) in order to obtain maximum dynamic range. The sensitometer spots with high densities were also measured in this way, to avoid calibration errors at high intensities. In addition, a field of 4×4 cm^2, centred on the region with the spots, was digitized to record the low density spots and the local fog levels (the latter were necessary for the construction of the calibration curve ; Sect. 3). It took about 40 hours to scan one plate. Lamp calibrations were obtained at the beginning and at the end of this period to check for drifts in intensity ; expressed in density units such drifts were found to be less than 0.005.

Unfortunately, some of the exposures have poor image quality due to flexure in the optics of the telescope (occurring in long exposures at large hour angles) and due to problems on one night with the focus setting of the telescope. For global surface photometry of M31 the plates with poor images are still useful, but they could not be included in the final stacked maps.

To summarize, the digitized data for each plate consist of :

(1) Two fields with 2048×2048 pixels of 40 μm^2, covering M31 and a substantial region around it (40 μm corresponds to 3.″864; 1″ to 3.3 pc).

(2) Several smaller fields, adjacent to the two large ones (Fig. 1), measured to obtain sky area sufficient for background correction.

(3) Small fields with pixels of 40×40 μm^2 centred on the nucleus of M31, on M32, and on NGC 205. These fields were measured with a high repetition factor in order to increase the dynamic range.

(4) Small maps with 50×50 pixels of 40×40 μm^2 centred on individual calibration spots.

(5) A large field with 1024×1024 pixels of 40×40 μm^2 centred on the region with the calibration spots which was scanned to record the fog level.

To reduce the total amount of data, most subsequent reduction and analysis of the two main fields was done after further compression to maps with 1024×1024 pixels of 80×80 μm^2.

3. Calibration.

3.1 SKY BACKGROUND EVALUATION. — It is important to consider the origin of sky variations on the plates, in order to judge whether they are additive (e.g. intrinsic sky intensity variations), or multiplicative (e.g. sensitivity variations). For additive sky variations the relative intensity of the galaxy, I_g, is derived from a straightforward sky subtraction :

$$I_g(x, y) = I_{g+\mathrm{sky}}(x, y) - I_{\mathrm{sky}}(x, y) . \qquad (1)$$

For multiplicative errors, the relative intensity of the galaxy is derived after a « flat fielding » correction such as used for modern electronic detectors :

$$I_g(x, y) = \frac{I_{g+\mathrm{sky}}(x, y) - I_{\mathrm{sky}}(x, y)}{I_{\mathrm{sky}}(x, y)} . \qquad (2)$$

(Strictly speaking this correction can only be applied this way for sky-limited exposures). The difference between these two sky-subtraction techniques is usually negligible in photographic photometry, because sky variations over the relevant region are at most a few percent. However, for plate areas as large as 10×20 cm^2 this is not necessarily the case, and it is necessary to assess the nature of the sky variations that are present before deciding on which sky subtraction to use.

We produced low resolution maps of the digitized data to enhance the sensitivity to weak, extended structures. The high resolution maps were divided into submatrices of 32×32 pixels (2.56×2.56 mm^2). In each submatrix the background level was determined by kappa-sigma clipping (see Appendix). The background levels of the

submatrices determined in this way were then combined to produce one low resolution map for each plate with only 160 × 100 pixels. This method of mapping the sky background is rapid and results in reduction of the number of data points, in noise suppression, and in removal of foreground stars. The low resolution maps proved to be useful, not only for assessing the sky background variations, but also for making sky fits (which would have been needlessly time consuming on the full resolution data), and for studying the structure of the galaxy at low light levels (Walterbos and Kennicutt, 1985).

In what follows we first discuss the large-scale variations of the sky background and the magnitude of the effects on our data as derived from an assessment of the low resolution maps and the sky fit procedure described below.

(1) All *R*, *F* and *V* exposures showed a strong increase in the sky background (10 % to 20 %) to the North, i.e. the direction of the Galactic plane. Hodge and Kennicutt (1982) mentioned a possible Galactic gradient accross their blue plate, but we found only minor effects on the *B* and *J* plates. As an independent check we scanned two (uncalibrated) Palomar Schmidt plates (a blue one and a red one), kindly provided by A. G. de Bruyn. These did not show a gradient in the expected sense. Further checks showed that the *V*, *R* and *F* plates were taken at rather large hour angles, and a correlation was found between the strength of the gradient and the average hour angle during exposure, suggesting a local night-sky brightness effect, perhaps due to the lights from Tucson. Thus the origin of the gradient could not be unambiguously determined, but it is probably a real intensity variation and it should therefore be treated as an additive error.

(2) The sensitivity of plates that are hypersensitized and then exposed through a filter that is close to the emulsion may vary significantly across the plate. The effect of hypersensitization decreases due to moist air that reaches the emulsion during exposure ; if the filter is close to the emulsion, the diffusion of air proceeds more rapidly at the edges of the (curved) plate than at the centre. The result is a decrease in sensitivity towards the edges of the plate. The effect was first found by Malin and is described by Campbell (1982) and by Dawe and Metcalfe (1982). The influence on the intensities seems to be a pure sensitivity variation, with no change in the slope of the characteristic curve. Wesselink (1987), however, pointed out possible changes in reciprocity failure, but these would mainly affect the low end of the calibration curve and are not important for sky-limited exposures. Possible evidence for the Malin effect was found on our *B* and *J* plates, which showed an increase in sky density, roughly towards the plate centre. Expressed in intensities, the increase was at most 5 % underneath the image of M31.

(3) Vignetting is a pure sensitivity variation. It causes a similar effect as the desensitization described above, but it is more confined to the corners of the plate (e.g. Campbell, 1982). We found no evidence in our evaluation of the background for this effect, but it might affect the outermost points along the major axis slightly.

(4) The influence of light scattered within the telescope was quantitatively examined. We measured the scattered light profile of the brightest star on the plates (ν And) and found it to be similar to the star profile derived for the Palomar Schmidt telescope by Kormendy (1973). Comparison of the original intensity distribution of M31 with that obtained after convolution with Kormendy's star profile, showed that scattered light is only important close to the minor axis at light levels below 26.5 mag arcsec^{-2} in *B*. At 27.8 mag arcsec^{-2} the intensity of the scattered light is comparable to the intensity of the galaxy itself. Because our photometry is not reliable in any case at such low light levels (see Sect. 4), scattered light is not a problem, especially when one considers that the little amount that may be present would be removed by our sky subtraction (Sect. 3.2).

In summary, the major deviations in the sky background are the gradients on the *R*, *F*, and *V* plates, which most likely result from real variations in the sky intensity. The next largest variation in sky, the possible Malin effect on our *B* and *J* plates, should be treated as a sensitivity variation. However, in view of the dominant effect of the gradient we decided to subtract sky according to expression (1). The resulting possible error in the blue intensities due to the Malin effect is at most 5 % across the galaxy, which is less than other sources of error discussed in section 4.

3.2 SKY FITTING. — The region used for the sky fit was selected on the low resolution maps where weak, extended emission from the galaxy can be traced easily. Regions contaminated by emission from M31, from the two companions, or from bright stars (including their scattered light halos) were deleted. In addition, regions close to the edge of the plate were deleted because some of the filters were round and did not cover these outer parts. The final region available for sky fitting encompassed about 35 to 40 % of the digitized part of the plate ; it is indicated in figure 1. We refer to this region as the « sky map ». At the outer portions of the major axis not much sky is available. Sky fitting was done on the sky map, in density units.

We tried several sky fitting techniques seeking one that could best represent the large-scale background variations described above. The simplest function, a flat plane, produced unsatisfactory results ; the resulting minor axis profile on the blue plates was much brighter for levels below sky intensity than the published photoelectric profiles. Higher order two-dimensional polynomial fits gave better results, but finally we adopted a

somewhat more complicated function, that could represent more variations in sky in the direction parallel to the major axis (where more information on sky variations is available (Fig. 1)) than in the direction perpendicular to the major axis (where a large gap has to be bridged).

The sky fitting procedure is illustrated schematically in figure 2. A second order two-dimensional polynomial was fit to part of the sky map, designated in figure 2 as box i. The fit was used to describe sky for the central strip (parallel to the minor axis and marked A) of the box. Then a new region was selected from the sky map, shifted to the right with respect to the previous region, but still largely overlapping with the previous region ; the new region is designated as box $i + 1$ in figure 2. A second order polynomial was fit to the new region and the resulting sky fit was used to describe sky for the central strip of box $i + 1$ (marked B). The strip in the new box was chosen adjacent to the strip in box i. Again, another region was selected by shifting the box to the right ; *mutatis mutandis*. To ensure continuity, the boxes were shifted each time by a small amount, corresponding to 1 to 2 mm on the plate. The fits for the first (leftmost) and last (rightmost) boxes were used for a larger part of the region enclosed by the boxes to obtain sky values for the outermost parts of the galaxy. This « moving box fit » reproduced the major deviations in the sky background well, without introducing spurious small scale structures in the fit underneath the galaxy. The amount of structure that can be represented is restricted by the width of the box. In practice, a width of 90 mm (almost half of the total width of the sky map) was used. The resulting sky fit was interpolated to the pixel size of the high resolution data and then subtracted, after conversion to intensities.

3.3 CONVERSION OF DENSITIES TO INTENSITIES. — The average densities of the spots and the surrounding fog levels were calculated from the digitized data using the method described in the Appendix. The low end of the characteristic curve is linearized effectively by plotting the logarithm of the opacitance or Baker density, and not the density itself, against the logarithm of the intensity (e.g. de Vaucouleurs, 1968). The opacitance, ω, is defined as :

$$\omega = 10^{(D - D_{\rm fog})} - 1 \,, \qquad (3)$$

where D is the density of the spot and $D_{\rm fog}$ is the density of the fog level close to the spot. A polynomial of the form :

$$\log(I) = \sum_{i=0}^{n} a_i (\log \omega)^i \,, \qquad (4)$$

was fit to the measured points (e.g. van der Kruit, 1979). In practice, a third or fourth order polynomial sufficed. From 10 to over 20 points were available to define the fit.

We had two different calibrations for the sensitometer that is in use with the Burrell Schmidt telescope. One we obtained shortly after the observing run by measuring the densities of the sensitometer wedge ; the other is the standard KPNO calibration that became available later on (Schoening, private communication). The two calibrations are not the same. Ours shows a significant color dependence ; the KPNO calibration is basically color independent. The increment in log (I) of the steps is systematically smaller in the KPNO calibration, resulting in a steeper calibration curve (γ's typically 20 % higher). The difference is largest in the blue and ultraviolet. We tested both calibrations to see which one gave the best results and to assess the differences in the photometry. The calibration that we used was selected on the basis of two criteria :

(1) The quality of the alignment of the two calibration curves that were obtained for those plates that had two sets of spots exposed on them.

(2) The agreement of our photometry with published photoelectric measurements. The match between the two calibration curves was good, usually slightly better with the KPNO calibration, except for the case of the U plates. The differences in photometric results were only significant (≥ 0.1 mag arcsec^{-2}) for bright levels within 2′ to 6′ from the nucleus. On average, the KPNO calibration gave better results, except for the U plates. Thus we used our own calibration for the U plates and the KPNO calibration for the others.

For all plates the two main fields (Sect. 2) with each 1024×1024 pixels of 80×80 μm^2, and the corresponding sky fit were converted to intensity using expression (1). Before subtracting the sky intensities from the total intensities, the parts of the large fields centred on the nucleus of M31, on M32, and on NGC 205 were replaced with the intensities from the small fields that were digitized with a high repetition factor. A lower resolution intensity map of the galaxy was obtained for each plate by compressing the two 1024×1024 intensity images to 160 μm^2 pixels and combining them into one image of 1024×512 pixels. The R surface brightnesses were not corrected for the presence of Hα emission ; the Hα intensities are low (Kennicutt *et al.*, in preparation) and contribute negligibly to the total intensity in the broad R band.

3.4 COMBINATION OF PLATES. — The quality of the individual plates was assessed from detailed comparisons of simulated aperture photometry on our data with the extensive set of published photometric data, and from comparisons between different plates in the same color band. In this way the reliability of long exposures at bright levels and of short exposures at faint levels was established. For a significant part of the galaxy both exposures could be used. Long and short exposures were then combined with a weighting factor appropriately

chosen for each surface brightness level. Both the images with 80×80 μm^2 pixels and the compressed images with 160×160 μm^2 pixels were combined in each color. Although usualy two long exposures were available in each color band (Tab. I), in general only one could be used because of the image problems mentioned in section 2. The exposures with poor images were, however, useful for establishing the reliability of the photometry (Sect. 4). For the final calibrated images in the various color bands only exposures that are not marked with an asterisk in table I were used. Thus the *U* image is obtained from only one plate, and the *B*, *J*, *V* and *R* images from two or three plates. Both *F* plates have image problems but we combined them anyway to have a check on the calibration of the *R* plates, which have very nearly the same color response.

3.5 REMOVAL OF FOREGROUND STARS. — Due to its large angular size and low galactic latitude ($-20°$), a huge number of foreground stars contaminates the field of M31. Based on the Bahcall-Soneira model for the Milky Way, Ratnatunga and Bahcall (1985) predict 52000 foreground stars with visual magnitudes between 13 and 21 in a field of 4 by 2 degrees in the direction of M31. Before the intensity of the galaxy can be studied, the foreground stars have to be removed. The large number of stars makes it necessary to do this in an automated way. The stars were removed on the final combined images with 80×80 μm^2 pixels and not on the individual plates, to save computing time.

Figure 3 shows a flow diagram of the procedure. Two basic steps were involved in the process. In the first step a low resolution intensity map (B) was produced from the original map (A), following the method that was used in the evaluation of the sky background (Sect. 3.1 and Appendix). In this step, all foreground stars and high resolution features in the galaxy are removed by severe kappa-sigma clipping. The low resolution map (B) was interpolated to the original pixel size and then subtracted from the original map (A), yielding a map (C) with only star images and compact features in M31, such as dust lanes and bright stellar associations. In the second step we applied more modest kappa-sigma clipping on relatively small submatrices in this map (C) and replaced all pixels that differed by more than a certain factor *G* times the r.m.s. deviation from the final mean intensity in the submatrix (obtained after a few iterations) with that mean value. The output of this step was a map (D) in which the stellar images were clipped. This map was subtracted from the map that was used as input to the second step (C), yielding a map with only stars in it and a background exactly equal to zero. This « star map » (E) was subtracted from the original intensity map, resulting in a final map (F) containing no stellar images anymore. The advantage of using two steps is that in the first phase the gradient in the background due to the presence of M31 is removed, so that in the second phase the clipping is done on a much more uniform map.

It is unavoidable that in an automatic routine such as this, high resolution structures in the galaxy are also clipped. The extent to which this occurs depends on the number of iterations used in the kappa-sigma clipping routine, the size of the submatrices, and the factor *G* used for the comparison of the intensity of a pixel with the mean intensity in the submatrix. The influence of foreground stars on the photometry depends on the intensity level of the light of the galaxy that one is trying to measure. At relatively bright levels only brighter foreground stars are important ; at faint levels both bright and faint stars affect the photometry. Therefore we obtained two star-subtracted images for each color. In one image only modest clipping was applied in the second step ($G = 3$, only one iteration) with the result that bright foreground stars were largely removed, while structures in the galaxy were hardly affected. These maps can be used to study the galaxy at levels brighter than about 24.0 mag arcsec^{-2} in the *B* band. A second image was obtained in which more severe clipping was applied in the second step ($G = 2$, three iterations) to remove basically all stars. On these maps the structure of the galaxy could be studied to much deeper levels. Radial profiles (Sect. 5) were obtained from these images. We will refer to the heavy clipping as « rigorous star removal » in the remainder of the paper.

The importance of the correction for foreground stars and the success of our method are best illustrated in a few figures. Figure 4 shows two major axis profiles in *R*, one obtained from the original image, the other from the image to which rigorous star removal was applied. A 60″ aperture was used. The difference between the two profiles is shown as well. The dominant role of foreground stars at faint levels is obvious from this figure. It is clear that for apertures much larger than 60″ weak foreground stars would no longer be visible as individual peaks. This may have affected the photometry by de Vaucouleurs (1958) who used an aperture of 138″. The influence on the structure of the galaxy can be assessed from a comparison of figure 5(a), which shows a *J* magnitude map with foreground stars still present, with figure 5(b), which shows the same map after rigorous star removal.

4. Absolute calibration and evaluation of the accuracy of the photometry.

4.1 COMPARISON WITH PUBLISHED PHOTOMETRIC DATA. — The first photometric measurements of the large scale light distribution in M31 data back to the thirties (Stebbins and Whitford, 1934 ; Redman and Shirley, 1937). Major studies based on one-dimensional tracings of photographic plates or photoelectric drift scans were done by Fricke (1954) in three colors, by de

Vaucouleurs (1958) mainly in the blue, by Lyngå (1959) in P and V, and by Burgess (1976) in four colors. Richter and Högner (1964) presented isophotal maps of M31 and the two companions, derived from equidensitometry on Schmidt plates. Of the more recent work we mention Hoessel and Melnick's (1980) three-color photometry of the SW major axis and the minor axis, Sharov and Lyutyj's (1980) *UBV* study of the bulge region, and the near-infrared scans of the East-West axis made by Hiromoto *et al.* (1983). Kent presented CCD photometry of a field of $3' \times 5'$ centred on the nucleus. For a complete listing of all photometric measurements of M31 and its companions we refer to Longo and de Vaucouleurs (1983), Davoust and Pence (1982), and Pence and Davoust (1985).

We compiled major, minor, and East-West axis profiles of M31 in various colors from all published data which give photometry extending to at least 5′ from the centre. Table II lists these data and indicates the colors and the extent along each of the axes. Small positional differences exist amongst the various data, due to the different position angles adopted for the major axis, or due to small positioning errors. In addition, various aperture sizes were used. The differences in the color bands amongst the various sets are also significant. This all means that in the comparisons of our data with the published material, the scatter is not all due to photometric errors, but mainly to these effects. Only systematic differences such as gradients provide information on the calibration accuracy. A few of the sets deserve special attention.

We found a difference of 0.6 mag in Lyngå's (1959) paper between the scale of his figure 4, which shows the profiles obtained from his plate group a, and the scale of his figure 6, which shows the profiles from his plate group b. Positional errors were found in the data of Hoessel and Melnick (1980), presumably from the problems which they cite with one of the telescope drive rates. Foreground stars and dust lanes made it possible to determine the positional error for their major axis profile. Their positions with respect to the centre have to be multiplied by a factor 1.035. Figure 8 suggests that a positional error is also present in their minor axis profile, but no structures are present in the profile which would have allowed a determination of the positional error. The scans from Burgess (1976) were available to us only in the form of rather poor quality plots ; the surface brightnesses could be measured from these plots to an accuracy of no more than $\pm$ 0.1 mag arcsec^{-2}. Therefore the scatter in the comparison of our data with his points is considerable. The near-infrared photometry by Matsumoto *et al.* (1977) and by Hiromoto *et al.* (1983) is included in table II for completeness. The color difference between our R band and their I band is so considerable that comparison of the two was not very useful. The general trend of progressively bluer colors with increasing distance along the axes (see Sect. 5) was, however, confirmed.

We compared our data with the published profiles, both for individual plates and for the combined images. Several representative examples are shown in figures 6 to 9. The internal consistency of our data can be assessed from comparisons between our B and J band images (roughly comparable color bands), and between our R and F band images (essentially identical color bands). Considering that the figures show direct comparisons for one-dimensional scans with no averaging involved (other than that implied by the size of the aperture) the agreement between our photometry and the published data seems satisfactory. The agreement between the various sets of published data can also be assessed from these scans. Figure 6(a) shows that our B photometry agrees with de Vaucouleurs's (1958) photometry down to at least 25.0 mag arcsec^{-2}. The apparent disagreement between $-50'$ to $-80'$ is mainly the result from the slightly different position angle for the major axis (37°.7) adopted by de Vaucouleurs, from the correction for stars in our data, and from the larger aperture (138″) used by de Vaucouleurs. For levels below 25.0 mag arcsec^{-2} along the major axis (not shown here) our B profile falls off more rapidly than de Vaucouleurs's profile, but this is at least partly due to the correction for foreground stars (Sect. 3.5). The comparison shown in figure 6(b) for the minor axis shows a significant disagreement near $-40'$. This difference was indicated by all our plates ; it may be caused by the ghost image of the bulge of M31 on our plates (see Fig. 5(b)). The agreement for the other colors (Figs. 7 to 9) is satisfactory. The estimated accuracy of our photometry is discussed in the next section.

The shift that was applied to the published data to obtain a zero average difference with our data is indicated in table II. The absolute zero level of our photometry was set by comparison with those published data that were on the Johnson *UBV* system : Burgess's (1976) scans, Sharov and Lyutyj's (1980) scans, and de Vaucouleurs's (1958) photometry. The offsets listed in table II show that the zero points of these three sets of material agree well. The zero point errors for our data, listed in table III, are based on the offsets that were found for each of the three axes (the offsets in Tab. II are the averages for the three axes). The zero point of our R photometry is not very well determined. It is based on the color equations from Jensen *et al.* (1981), adopting a V-(Johnson) R for the bulge of 0.8.

4.2 EVALUATION OF PHOTOMETRIC ACCURACY. — The photometric accuracy of our data was estimated in different ways, depending on the surface brightness level of the galaxy. Two ranges can be distinguished. For levels above sky intensity (about 21.8 mag arcsec^{-2} in B) the uncertainties are determined by errors in the cali-

bration curve. These uncertainties were estimated empirically from plate/plate comparisons and from comparisons with the published data. At levels below sky intensity, the uncertainties are mainly determined by errors in the subtracted sky intensities. These errors were estimated from the distribution of intensities in the region that was used to define the sky fit, after this sky fit has been subtracted. In general the residuals show an r.m.s. dispersion between 1 and 1.5 % of the sky intensity. The characteristic scale size of the residuals is a few cm on the plate. These plate nonuniformities are probably a result of the developing process, which is never ideal. Halos of star images and ghost images of stars contribute as well to the nonuniformity. We calculated the r.m.s. dispersion of sky residuals for each color and the corresponding uncertainties at various surface brightness levels. To this error we added quadratically the errors that might be introduced by having used expression (1) to subtract sky and not expression (2) (see Sect. 3.1 ; note that these errors can be calculated from the sky fit). The total uncertainties for each color are listed in table III as a function of surface brightness in that color. Zero point errors, determined as described above, are listed separately. The errors refers to the systematic deviations that may be present in the data over distances of half a degree or more, not to the pixel-to-pixel noise. For the *U* plate the uncertainties are largest ; only one good plate was available and the galaxy is relatively faint in *U*. The estimated errors in *V* and *R* are larger than in *B*, because sky nonuniformities are more severe on the IIaD and 098 emulsions. Over the part of the optical disk that is generally visible on optical photographs, the maximum errors in surface brightness vary between ± 0.06 mag arcsec^{-2} in *B* to ± 0.15 mag arcsec^{-2} in *U*. For fainter levels the errors increase exponentially.

We calculated the total magnitudes of M31 from our data by summing the intensities in a large rectangle, extending beyond the galaxy and centred on the nucleus. The intensities in smaller rectangles, each encompassed by the previous larger rectangle, were also obtained. A growth curve can be constructed in this way and the total intensity of the galaxy, corrected for the presence of foreground stars, can be determined from a plot of the sum of the intensities in each rectangle against the number of pixels in that rectangle, by linear extrapolation of the points to zero pixels. The contribution from the elliptical companions, amounting to a few percent of the total flux, was subtracted. The results are listed in table IV. The estimates of the uncertainties refer to the errors in the zero level of the maps and not to the errors in the intensity calibration. The total magnitudes that we derive are in good agreement with the values taken from the RC2 catalog (de Vaucouleurs *et al.*, 1976). We also derived the colors of the elliptical companions, NGC 205 and M32. For NGC 205 our values agree well with published results. We find a *B-V* of 0.77 and a *U-B* of 0.30, while Price and Grasdalen (1983) found *B-V* = 0.73, *U-B* = 0.30, and the RC2 values are *B-V* = 0.84, *U-B* = 0.20 (de Vaucouleurs *et al.*, 1976). For M32 our values are *B-V* = 0.88, *U-B* = 0.31, while the RC2 lists *B-V* = 0.94, *U-B* = 0.47. The difference in *B-V* is well within our errors, but we have no explanation for the relatively blue *U-B* color that we derive.

5. Results.

We provide here some quantities which are important for comparisons of the distribution of other components in M31 with the optical light distribution. In table V we list *U, B, V*, and *R* profiles for the major, minor, and West-East axes of the galaxy. The intensities were obtained by simulated aperture photometry through 60″ and 120″ circular diaphragms. No corrections were applied for foreground extinction. The influence of foreground stars was eliminated as much as possible by using the appropriate star-subtracted images, discussed in section 3.5, for each surface brightness level. The profiles are shown in figure 10.

Two-dimensional color maps, obtained using images from which the brighter stellar images were removed, are shown in figure 11. In addition to the standard *U-B* and *B-V* images, we have included the (independent) images of the *U-V* and *B-R* indexes. The *U-V* image shows the OB associations most clearly ; dust lanes are better visible in the other color maps.

The colors of the bulge and the inner disk out to roughly 9 kpc (45′) are rather constant, with a *B-V* index between 0.9 and 1.0 and a *U-B* index between 0.45 and 0.55 (not corrected for extinction). These colors are typical for an old stellar population. For distances beyond 9 kpc the colors get bluer with increasing distance to the centre, which is undoubtedly largely due to the presence of young stars in spiral arms. The ring of Population I material near 10 kpc is conspicuous in the color maps. Spiral arm crossings are apparent in the major axis profile (Fig. 10(a)). The blue peak near $-40'$ corresponds to the brightest OB association in M31, NGC 206. Dust lanes on the near (West) side of M31 can be recognized on cuts along the minor and West-East axes (Fig. 10(b) and 10(c)) as a significant reddening of the colors. The extinction in the dust lanes will be analysed in a forthcoming paper.

The effect of nonuniformities in the sky background can be reduced by azimuthal averaging of the light distribution. We obtained the global light profile of M31 by averaging in elliptical rings the light distribution on the maps to which rigorous star removal was applied. An inclination of 77° was assumed. Due to the large inclination of M31 severe projection effects are present. As a

result of the finite thickness of the stellar disk and, especially, the presence of the bulge, the minor axis profile is brighter than the major axis profile, even after correction for the foreshortening due to the inclination. Nevertheless, the average profile should give a more reliable indication of the colors far out in the disk ; it is furthermore useful for comparison with other galaxies for which often only a global profile is available. The results are listed in table VI and displayed in figure 12. The intensities have *not* been scaled to a face-on projection. The colors get continuously bluer with increasing distance out to at least 20 kpc (100′).

An impression of the overall structure and extent of the galaxy can be obtained from the *J* magnitude map shown in figure 5(b). On the Southern major axis a change in position angle occurs around − 100′, which seems to indicate a warping of the stellar disk, in agreement with the results from Innanen *et al.* (1982 ; see also Walterbos and Kennicutt, 1985). Striking in figure 5(b) is the twisting of the isophotes of the elliptical companion NGC 205 (to the bottom), which suggests tidal interaction with M31.

Acknowledgements.

It is a pleasure to thank R. le Poole for useful discussions and for advice concerning the use of the Astroscan, and F. van Rooyen for keeping the machine going. Some of our software was based on routines kindly made available to us by P.C. van der Kruit and installed in Leiden by A. Bosma.

R. C. Kennicutt acknowledges support from NSF Grant AST81-11711A01 and from an Alfred P. Sloan Fellowship. In addition he acknowledges a visitors grant from the Netherlands Organization for the Advancement of Pure Research (ZWO) during the initial stages of this project. R. A. M. Walterbos was supported by the Netherlands Foundation for Astronomical Research (ASTRON) with financial aid from ZWO.

Appendix. Local background determination.

In a number of steps in the reduction of our material, a local background value of (part of) a digitized area had to be established, for example in the calculation of the average densities of the sensitometer spots, in the determination of the sky level values around M31, and in the photometry of M31 itself, where we have to correct for the presence of foreground stars. A useful method for determining a local background value in a field contaminated by stars or by plate defects such as scratches or holes in the emulsion, is an iterative procedure called kappa-sigma clipping. This method has been described elsewhere (e.g. Newell, 1979), so we will only outline the principal aspects. For the region of interest, the mean sky background and r.m.s. dispersion are calculated. Next, all points deviating more than twice the dispersion from the mean, either in positive or negative sense, are deleted and a new mean and dispersion are calculated. This procedure is repeated a few times and usually converges very rapidly to a mean that is essentially equal to the median of the histogram of the distribution of densities in the region of interest. For the method to work, the noise distribution has to be symmetrical. This is the case for photographic plates where the noise distribution has a Gaussian shape. To remove the halos of stars better, we built in the option that in the last iteration not only the one pixel that deviated too much was deleted, but also its four closest neighbouring points.

Newell (1979) discussed the reliability of the method for various fractions of contaminated pixels in the region of interest. For heavy contamination, occurring for example when a large number of foreground stars is present in the region, the final mean may be slightly higher than the true background level. This is not a problem, however, because to first order the background levels are affected in a similar way as the light intensity of the galaxy. Thus, a slight overestimate of the sky background in the sky subtraction will not affect the photometry at low levels, because the light of the galaxy is also overestimated. (Remember that our star subtraction technique (Sect. 3.5) is also based on kappa-sigma clipping).

References

BAADE, W., SWOPE, H. H. : 1963, *Astron. J.* **68,** 435.
BERKHUIJSEN, E. M., WIELEBINSKI, R., BECK, R. : 1983, *Astron. Astrophys.* **117,** 141.
BRINKS, E., SHANE, W. W. : 1984, *Astron. Astrophys. Suppl. Ser.* **55,** 179.
BURGESS, R. D. : 1976, Ph. D. thesis, University of Indiana.
BYSTEDT, J. E. V., BRINKS, E., DE BRUYN, A. G., ISRAEL, F. P., SCHWERING, P. B. W., SHANE, W. W., WALTERBOS, R. A. M. : 1984, *Astron. Astrophys. Suppl. Ser.* **56,** 245.
CAMPBELL, A. W. : 1982, *The Observatory* **102,** 195.
DAVOUST, E., PENCE, W. D. : 1982, *Astron. Astrophys. Suppl. Ser.* **49,** 631.
DAWE, J. A., METCALFE, N. : 1982, *Proc. ASA* **4** (4), 466.

DE VAUCOULEURS, G. : 1958, *Astrophys. J.* **128,** 465.
DE VAUCOULEURS, G. : 1968, *Appl. Optics* **7,** No 8, p. 1513.
DE VAUCOULEURS, G., DE VAUCOULEURS, A., CORWIN, H. G. : 1976, Second Reference Catalog of Bright Galaxies, *Univ. Tex. Monogr. Astron.* **2.**
FRICKE, W. : 1954, *Zeitschr. Astrophys.* **34,** 137.
HABING, H. J., MILEY, G., YOUNG, E., BAUD, B., BOGGESS, N., CLEGG, P. E., DE JONG, T., HARRIS, S., RAIMOND, E., ROWAN-ROBINSON, M., SOIFER, B. T. : 1984, *Astrophys. J. Lett.* **278,** L59.
HIROMOTO, N., MAIHARA, T., ODA, N., OKUDA, H. : 1983, *Publ. Astron. Soc. Jpn* **35,** 413.
HODGE, P. W., KENNICUTT, R. C. : 1982, *Astron. J.* **87,** 264.
HOESSEL, J., MELNICK, J. : 1980, *Astron. Astrophys.* **84,** 317.
INNANEN, K. A., KAMPER, K. W., PAPP, K. A., VAN DEN BERGH, S. : 1982, *Astrophys. J.* **254,** 515.
JENSEN, E. B., TALBOT, R. J., DUFOUR, R. J. : 1981, *Astrophys. J.* **243,** 716.
KENT, S. M. : 1983, *Astrophys. J.* **266,** 562.
KORMENDY, J. : 1973, *Astron. J.* **78,** 255.
LONGO, G., DE VAUCOULEURS, A. : 1983, *Univ. Tex. Monogr. Astron.* **3.**
LYNGÅ, G. : 1959, *Medd. Lunds Astron. Obs.* **2,** No 137.
MATSUMOTO, T., MURAKAMI, H., HAMAJIMA, K. : 1977, *Publ. Astron. Soc. Jpn* **29,** 583.
NEWELL, E. B. : 1979, in *Image Processing in Astronomy,* G. Sedmak, M. Capaccioli, R. J. Allen (Eds) (Oss. Astron. di Trieste), p. 100.
PENCE, W. D., DAVOUST, E. : 1985, *Astron. Astrophys. Suppl. Ser.* **60,** 517.
PRICE, J. S., GRASDALEN, G. L. : 1983, *Astrophys. J.* **275,** 559.
RATNATUNGA, K. U., BAHCALL, J. N. : 1985, *Astrophys. J. Suppl. Ser.* **59,** 63.
REDMAN, R. O., SHIRLEY, E. G. : 1937, *Mon. Not. R. Astron. Soc.* **97,** 416.
RICHTER, N., HÖGNER, W. : 1964, *Astron. Nachr.* **287,** 261.
RYDEN, B. S., STARK, A. : 1986, *Astrophys. J.* **305,** 823.
SHAROV, A. S., LYUTYJ, V. M. : 1980, *Astron. Zh.* **57,** 449 (*Sov. Astron.* **24,** 259, 1980).
STARK, A. : 1985, in *The Milky Way Galaxy* (*IAU Symp.* **106**), H. van Woerden, R. J. Allen, W. B. Burton (Eds) (Reidel Dordrecht), p. 445.
STEBBINS, J., WHITFORD, A. E. : 1934, *Proc. Nat. Acad. Sci.* **20,** 93.
SWAANS, L. W. J. G. : 1981, Ph. D. thesis, University of Leiden.
TALBOT, R. J., JENSEN, E. B., DUFOUR, R. J. : 1979, *Astrophys. J.* **229,** 91.
UNWIN, S. C. : 1980a, *Mon. Not. R. Astron. Soc.* **190,** 551.
UNWIN, S. C. : 1980b, *Mon. Not. R. Astron. Soc.* **192,** 243.
VAN DER KRUIT, P. C. : 1979, *Astron. Astrophys. Suppl. Ser.* **38,** 15.
VAN DER KRUIT, P. C., SEARLE, L. : 1981, *Astron. Astrophys.* **95,** 116.
WALTERBOS, R. A. M., BRINKS, E., SHANE, W. W. : 1985, *Astron. Astrophys. Suppl. Ser.* **61,** 451.
WALTERBOS, R. A. M., KENNICUTT, R. C. : 1985, in *New Aspects of Galaxy Photometry,* Proc. of the VIIIth European Regional I.A.U. Meeting, Toulouse, 1984, J.-L. Nieto (Ed.) (Springer Verlag), p. 245.
WALTERBOS, R. A. M., SCHWERING, P. B. W. : 1987, *Astron. Astrophys.,* in press.
WESSELINK, T. : 1987, Ph. D. thesis, University of Nijmegen.

TABLE I. — *Burrell Schmidt plates of M31.*

plate number	color	emulsion and filter	exposure time (min.)	date September 1981
6770*	U	IIaO + UG2	120	24/25
6775	U	IIaO + UG2	120	25/26
6771*	B	IIaO + GG385	40	24/25
6774	B	IIaO + GG385	45	25/26
6776	B	IIaO + GG385	5	25/26
6772*	V	IIaD + GG495	45	24/25
6773	V	IIaD + GG495	45	25/26
6778	V	IIaD + GG495	5	25/26
6763	R	098-04 + RG610	40	23/24
6765	R	098-04 + RG610	5	23/24
6783	R	098-04 + RG610	42	26/27
6769	J	IIIaJ + GG385	90	24/25
6777	J	IIIaJ + GG385	10	25/26
6782*	J	IIIaJ + GG385	110	26/27
6768*	F	IIIaF + RG610	120	24/25
6779*	F	IIIaF + RG610	120	25/26

(*) used for checks on calibration only.

TABLE II. — *Photometric comparison data.*

reference	color	range in intensity (mag $''^{-2}$)	range in position major axis (')	minor axis (')	W/E axis (')	offset[a] (mag $''^{-2}$)
1. Lyngå (1959)	P	18.0 - 23.4	- 40,+40	-17,+17	-	+0.18
	V	17.0 - 22.7	- 32,+40	-17,+17	-	+0.04
2. Fricke (1954)	u	20.4 - 24.5	- 34,+50	- 9,+14	-	-1.23
	b	18.6 - 23.9	- 40,+56	-17,+17	-	-0.17
	r	18.2 - 22.5	- 37,+56	-17,+17	-	-0.61
3. Sharov and Lyutyj (1980)	U	19.0 - 22.8	- 5,+ 5	- 5,+ 5	- 5,+ 5	+0.02
	B	18.4 - 22.2	- 5,+ 5	- 5,+ 5	- 5,+ 5	+0.03
	V	17.4 - 21.0	- 5,+ 5	- 5,+ 5	- 5,+ 5	+0.08
4. Burgess (1976)	U	18.9 - 24.0	- 60,+50	-20,+15	-20,+20	+0.03
	B	18.0 - 24.5	- 60,+50	-20,+15	-20,+20	-0.04
	V	17.1 - 24.0	- 60,+50	-20,+15	-20,+20	-0.05
	I	15.6 - 20.2	- 10,+10	-13,+13	-10,+10	+1.10
5. de Vaucouleurs (1958)	U	22.1 - 24.9	-	-	-28,+24	-0.07
	B	21.5 - 26.8	-120,120	-58,+38	-44,+42	+0.02
	V	20.8 - 24.6	-	-	-33,+35	-0.02
6. Hoessel and Melnick (1980)	v	17.9 - 22.9	- 44,- 1	- 8,+10	-	+0.40[b]
	g	17.0 - 22.3	- 44,- 1	- 8,+10	-	+0.65
	r	17.4 - 21.8	- 44,- 1	- 8,+10	-	-0.51
7. Hiromoto et al. (1983)	I'	5 mag	-	-	-19,+19	
8. Matsumoto et al. (1977)	I	17.0 - 20.1	-	-	-11,+14	+0.85

([a]) difference between our adopted absolute calibration and the magnitude scale of the published data (ours-pub).
([b]) offsets only based on comparison for major axis.

TABLE III. — *Estimated uncertainties.*

surface brightness (mag arcsec^{-2})	U	B	V	R
17.0	-	-	±0.10	±0.15
18.0	-	±0.10	0.05	0.10
19.0	±0.15	0.05	0.05	0.06
20.0	0.08	0.05	0.05	0.07
21.0	0.06	0.05	0.05	0.08
22.0	0.07	0.06	0.07	0.09
22.5	0.07	0.06	0.09	0.12
23.0	0.08	0.06	0.12	0.15
23.5	0.10	0.07	0.15	0.17
24.0	0.15	0.08	-0.18,+0.22	0.25
24.5	0.22	0.10	-0.3, +0.4	-0.3, +0.4
25.0	-0.3, +0.4	0.15	-0.5, +0.7	-
25.5	-0.5, +0.7	-0.16,+0.22	-	-
26.0	-	-0.2, +0.3	-	-
26.5	-	-0.4, +0.6	-	-
zero point error	±0.05	±0.05	±0.07	-

TABLE IV. — *Integrated apparent magnitudes of M31.*

quantity	our value	zero point error (Table 3)	RC2 values (de Vaucouleurs et al. 1976)
m_U	4.75±.03	±0.05	
m_B	4.38±.03	±0.05	4.36
m_V	3.47±.03	±0.07	
m_R	2.76±.03		
U-B	0.37		0.50
B-V	0.91		0.91

1987A&AS...69..311W

TABLE V(a). — *Major-axis profile of M31 in U, B, V and R.*

position SW	B	U-B	B-V	B-R	position NE	B	U-B	B-V	B-R	aperture
1'	18.53	-	-	-	1'	18.56	-	-	-	60"
2	19.32	-	0.96	1.79	2	19.32	-	0.97	1.77	
3	19.80	0.53	0.99	1.82	3	19.86	0.56	1.01	1.80	
4	20.21	0.50	1.01	1.81	4	20.25	0.53	1.03	1.81	
5	20.50	0.50	0.97	1.77	5	20.49	0.52	1.00	1.76	
6	20.76	0.49	0.97	1.77	6	20.82	0.54	1.02	1.80	
7	20.93	0.46	0.96	1.74	7	21.22	0.58	1.08	1.90	
8	21.16	0.49	0.97	1.76	8	21.25	0.51	1.02	1.80	
9	21.26	0.50	0.95	1.73	9	21.33	0.50	0.98	1.75	
10	21.37	0.54	0.93	1.71	10	21.46	0.45	0.99	1.75	
12	21.62	0.57	1.02	1.79	12	21.66	0.48	1.00	1.75	
14	21.60	0.46	0.96	1.70	14	21.67	0.45	0.98	1.74	
16	21.81	0.51	0.98	1.70	16	21.72	0.49	0.98	1.76	
18	21.93	0.53	0.95	1.68	18	21.82	0.46	0.97	1.77	
20	22.09	0.54	0.96	1.68	20	21.98	0.37	0.94	1.71	
22	22.53	0.60	1.06	1.78	22	22.22	0.51	0.99	1.78	
24	22.41	0.55	0.97	1.65	24	22.24	0.56	1.01	1.80	
26	22.70	0.63	1.08	1.76	26	22.43	0.50	1.02	1.80	
28	22.75	0.50	1.05	1.72	28	22.75	0.44	1.09	1.84	
30	22.76	0.43	1.00	1.71	30	22.63	0.45	0.99	1.72	
32	22.75	0.46	0.99	1.69	32	22.78	0.42	1.03	1.76	
34	22.71	0.47	0.96	1.62	34	22.82	0.35	1.01	1.72	
36	22.97	0.47	1.05	1.75	36	22.84	0.36	1.00	1.72	
38	22.81	0.29	0.91	1.66	38	22.92	0.43	1.02	1.78	
40	22.23	0.06	0.73	1.40	40	23.05	0.36	1.05	1.84	
43	22.80	0.16	0.83	1.54	43	22.91	0.26	0.97	1.73	120"
46	22.75	0.15	0.83	1.46	46	22.86	0.21	0.93	1.69	
49	22.97	0.21	0.85	1.51	49	23.15	0.18	0.98	1.78	
52	23.12	0.30	0.88	1.48	52	23.17	0.17	0.86	1.66	
55	23.44	0.32	0.90	1.57	55	23.31	0.23	0.90	1.61	
58	23.65	0.42	0.86	1.55	58	23.50	0.27	0.95	1.64	
61	23.75	0.37	0.83	1.55	61	23.86	0.08	0.97	1.62	
64	23.74	0.47	0.79	1.41	64	23.92	0.19	0.87	1.58	
67	23.99	0.37	0.82	1.50	67	23.70	0.04	0.70	1.41	
70	23.95	0.39	0.85	1.47	70	23.62	-0.30	0.60	1.36	
73	23.97	0.33	0.71	1.33	73	24.25	0.04	0.70	1.57	
76	24.26	-	0.76	1.38	76	24.45	-	0.72	1.46	
79	24.46	-	0.75	1.40	79	24.49	-	0.70	1.45	
82	24.42	-	0.8	1.4	82	24.49	-	0.5	1.3	
85	24.57	-	0.8	1.4	85	24.80	-	0.6	1.2	
88	24.63	-	0.7	1.4	88	25.2	-	0.5	1.3	
91	24.76	-	0.7	1.5	91	25.4	-	-	-	
94	24.94	-	0.6	1.4	94	25.5	-	-	-	
97	24.91	-	0.6	1.4	97	25.8	-	-	-	
100	25.8	-	-	-	100	25.9	-	-	-	

TABLE V(b). — *Minor-axis profile of M31 in U, B, V and R.*

position NW	B	U-B	B-V	B-R	position SE	B	U-B	B-V	B-R	aperture
1'	18.71	-	-	-	1'	18.74	-	-	-	60"
2	19.71	0.53	1.02	1.81	2	19.73	0.51	1.00	1.81	
3	20.49	0.55	1.06	1.87	3	20.37	0.47	1.00	1.79	
4	21.10	0.63	1.10	1.93	4	20.76	0.45	0.97	1.74	
5	21.89	0.70	1.22	2.09	5	21.18	0.44	0.97	1.74	
6	22.11	0.66	1.17	2.01	6	21.54	0.45	0.98	1.75	
7	22.07	0.55	1.06	1.86	7	21.71	0.40	0.91	1.67	
8	22.27	0.46	1.05	1.82	8	21.98	0.42	0.92	1.70	
9	22.89	0.62	1.15	1.92	9	22.13	0.35	0.90	1.64	
10	23.15	0.51	1.03	1.80	10	22.22	0.30	0.89	1.60	
12	23.20	0.45	1.05	1.82	12	22.76	0.31	0.98	1.70	
14	23.26	0.36	0.96	1.60	14	22.90	0.24	0.92	1.57	
16	23.35	0.41	1.01	1.58	16	23.36	0.33	0.89	1.53	
18	23.72	0.39	0.97	1.56	18	23.75	0.20	1.01	1.64	
20	24.00	0.30	1.03	1.50	20	24.21	0.35	0.99	1.57	
22	24.13	0.28	0.84	1.46	22	24.37	-	0.89	1.51	120"
24	24.22	0.25	0.78	1.40	24	24.74	-	1.03	1.60	
26	24.17	0.21	0.84	1.43	26	25.03	-	1.0	1.53	
28	23.90	0.26	0.80	1.40	28	25.2	-	1.0	1.6	
30	23.78	0.22	0.76	1.47	30	25.7	-	-	-	
32	23.32	0.23	0.82	1.50	32	25.9	-	-	-	
34	22.73	0.31	0.81	1.46	34	26.5	-	-	-	
36	23.03	0.34	0.82	1.48	36	26.5	-	-	-	
38	23.79	0.38	0.81	1.44						
40	24.21	0.36	0.82	1.41						
42	24.55	-	0.75	1.3						
44	24.94	-	0.8	1.4						
46	25.8	-	0.8	1.2						
48	26.1	-	-	-						
50	26.2	-	-	-						

TABLE V(c). — *West-East profile of M31 in U, B, V and R.*

position W	B	U-B	B-V	B-R	position E	B	U-B	B-V	B-R	aperture
1'	18.66	-	-	-	1'	18.51	-	-	-	60"
2	19.39	0.53	0.95	1.73	2	19.44	0.56	1.00	1.80	
3	20.07	0.53	1.03	1.82	3	20.03	0.51	1.04	1.84	
4	20.61	0.56	1.06	1.88	4	20.37	0.50	1.02	1.81	
5	21.13	0.61	1.12	1.95	5	20.70	0.50	0.98	1.77	
6	21.81	0.64	1.23	2.11	6	20.97	0.49	0.98	1.76	
7	22.26	0.70	1.26	2.15	7	21.20	0.48	0.97	1.76	
8	22.05	0.61	1.15	1.96	8	21.43	0.47	0.97	1.73	
9	22.01	0.53	1.04	1.82	9	21.62	0.48	0.94	1.70	
10	22.22	0.53	1.03	1.78	10	21.87	0.46	0.95	1.70	
12	23.16	0.46	1.07	1.78	12	22.16	0.35	0.87	1.62	
14	22.96	0.42	1.00	1.71	14	22.26	0.26	0.82	1.50	
16	23.42	0.46	1.04	1.72	16	22.54	0.22	0.85	1.58	
18	23.40	0.40	0.95	1.54	18	22.80	0.28	0.88	1.58	
20	23.57	0.37	0.92	1.56	20	23.04	0.33	0.82	1.52	
22	23.72	0.37	0.94	1.53	22	23.64	0.31	0.83	1.64	120"
24	23.93	0.33	1.01	1.51	24	23.95	0.35	0.94	1.65	
26	24.23	0.3	1.05	1.50	26	24.28	0.2	0.93	1.65	
28	24.47	-	1.1:	1.5	28	24.54	-	0.9	1.7	
30	24.84	-	1.2:	1.5	30	24.85	-	0.9	1.7	
32	24.96	-	1.2:	1.3	32	25.2	-	0.9	1.8:	
34	25.2	-	-	-	34	25.4	-	-	-	
36	25.4	-	-	-	36	25.7	-	-	-	
38	25.5	-	-	-	38	25.9	-	-	-	
40	25.9	-	-	-	40	26.1	-	-	-	

TABLE VI. — *Average radial light profile of M31 in U, B, V and R.*

position	B	U-B	B-V	B-R	position	B	U-B	B-V	B-R
4'	19.53	0.58	0.97	1.77					
5	19.80	0.56	0.98	1.78					
6	20.04	0.54	0.99	1.79	58'	23.24	0.26	0.90	1.60
7	20.26	0.52	1.01	1.79	61	23.34	0.26	0.89	1.58
8	20.45	0.51	1.01	1.79	64	23.43	0.26	0.88	1.57
9	20.61	0.51	1.00	1.79	67	23.50	0.25	0.87	1.56
10	20.76	0.51	1.01	1.79	70	23.61	0.23	0.87	1.54
12	21.03	0.52	1.01	1.79	73	23.77	0.27	0.85	1.53
14	21.23	0.51	1.00	1.78	76	23.94	0.26	0.86	1.53
16	21.41	0.52	1.00	1.78	79	24.07	0.26	0.86	1.53
18	21.58	0.51	1.00	1.79	82	24.19	0.26	0.84	1.51
20	21.76	0.52	1.00	1.79	85	24.35	0.24	0.84	1.51
22	21.96	0.51	1.01	1.80	88	24.47	0.23	0.82	1.50
24	22.12	0.51	1.02	1.80	91	24.59	0.22	0.81	1.50
26	22.22	0.50	1.01	1.78	94	24.73	0.20	0.80	1.50
28	22.28	0.48	1.00	1.75	97	24.84	0.20	0.80	1.47
30	22.34	0.47	0.98	1.73	100	24.94	0.20	0.81	1.44
32	22.42	0.47	0.98	1.72	103	25.10	0.22	0.80	1.45
34	22.52	0.44	0.98	1.72	106	25.24	0.20	0.80	1.43
36	22.63	0.43	0.99	1.72	109	25.36	0.16	0.77	1.43
38	22.71	0.39	0.99	1.72	112	25.49	0.17	0.80	1.42
40	22.73	0.35	0.97	1.69	115	25.62	0.11	0.81	1.41
43	22.82	0.33	0.96	1.68	118	25.70	0.19	0.81	1.38
46	22.82	0.29	0.92	1.63	121	25.87	0.13	0.83	1.38
49	22.89	0.26	0.90	1.62	124	25.91	0.16	0.81	1.30
52	23.00	0.25	0.90	1.61					
55	23.13	0.26	0.91	1.62					

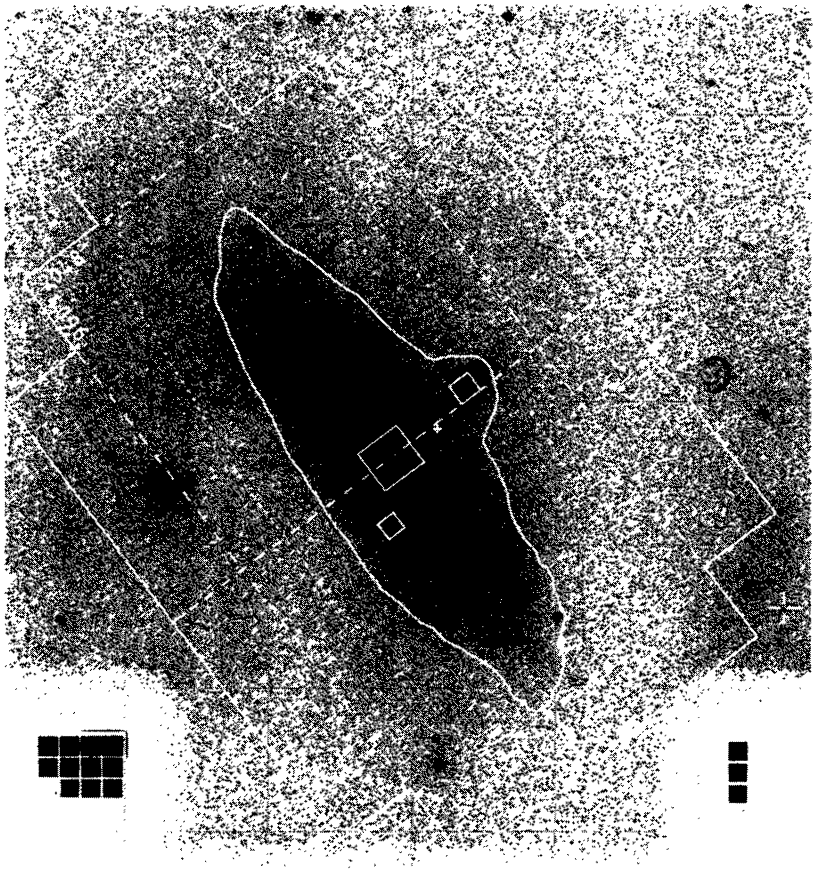

FIGURE 1. — Central 18 × 18 cm^2 of a blue plate of M31 taken with the Burrell Schmidt. The region that was digitized is indicated by the outer full-drawn white line. The dashed lines show the division in subfields. The central two large squares each consist of 2048 × 2048 pixels of 40 × 40 μm^2. The full-drawn contour corresponds roughly to the 25th mag arcsec^{-2} in *B*. The small regions centred on M31, M32 and NGC 205 that were digitized with a high repetition factor to increase the dynamic range of the Astroscan are also indicated. The dotted lines delineate the region that was used for sky fitting. The small cross marks the plate centre.

1987A&AS...69..311W

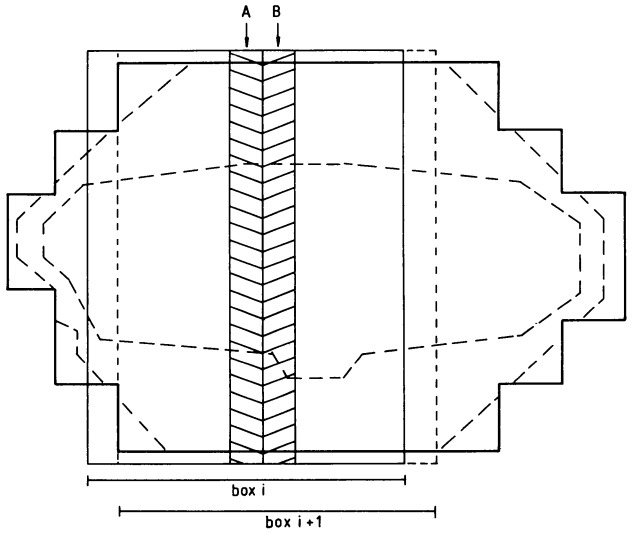

FIGURE 2. — Illustration of the sky fitting technique described in the text. The full drawn thick lines delineate the region that was scanned ; the long dashed lines the region used for sky fitting (cf. Fig. 1). The thin full drawn line marks the boundary of box i ; the thin dashed line the boundary of the next box. The hatched region marked A is the strip for which the sky fit determined in box i was used. Region B indicates the part for which the fit determined in box $i + 1$ was used. The boxes are drawn on roughly the same scale as the digitized region ; the width of strips A and B was much smaller in reality, as was the distance between box i and box $i + 1$.

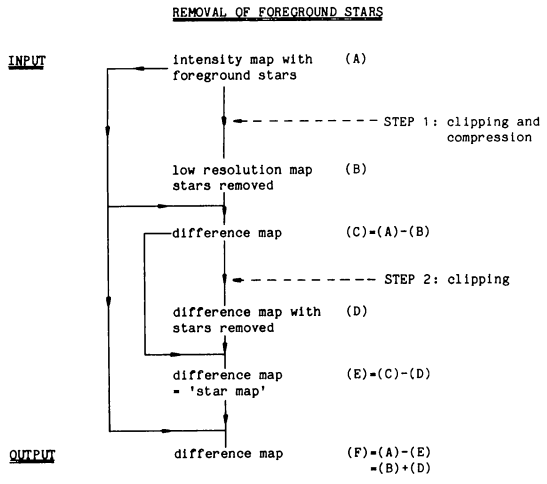

FIGURE 3. — Flow diagram of the star subtraction routine (see Sect. 3.5).

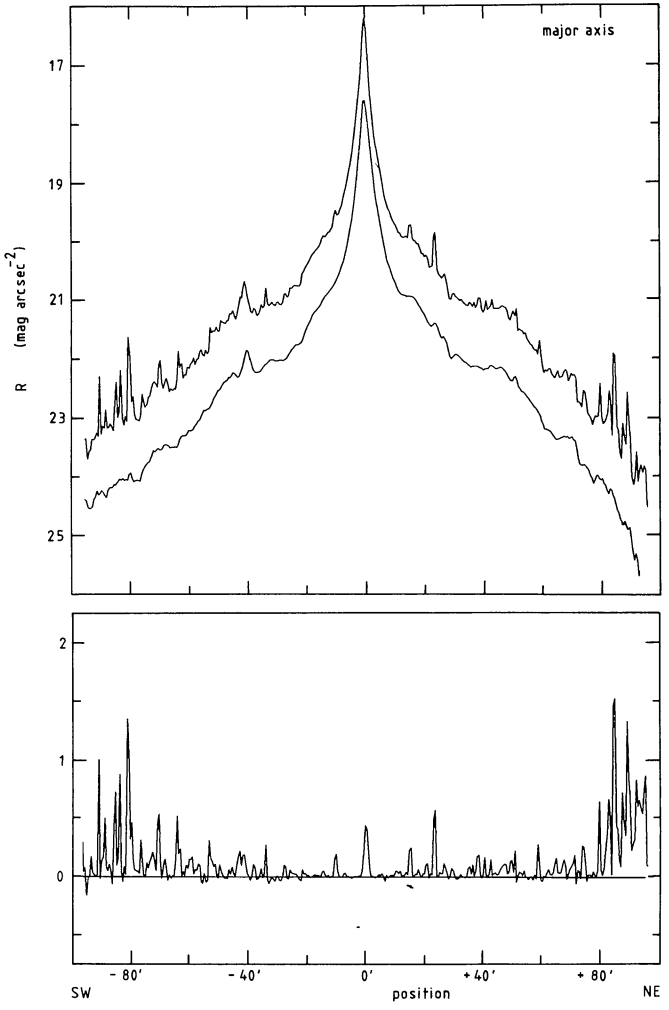

FIGURE 4. — The effect of foreground stars on the photometry. The top profile is a major axis R profile through a 60″ aperture with no correction for foreground stars. The bottom profile was obtained from the same data after « rigorous star removal » (see Sect. 3.5). It is shifted downwards by one magnitude. The bottom part of the figure shows the difference between the two. Obviously, for fainter light levels the influence of foreground stars becomes more and more important. For apertures larger than 60″ the weaker foreground stars would no longer be distinguishable in the top profile. In the rigorous, automatic routine that has been used for removing the stars, it is unavoidable that some of the high resolution structure in M31 is also clipped.

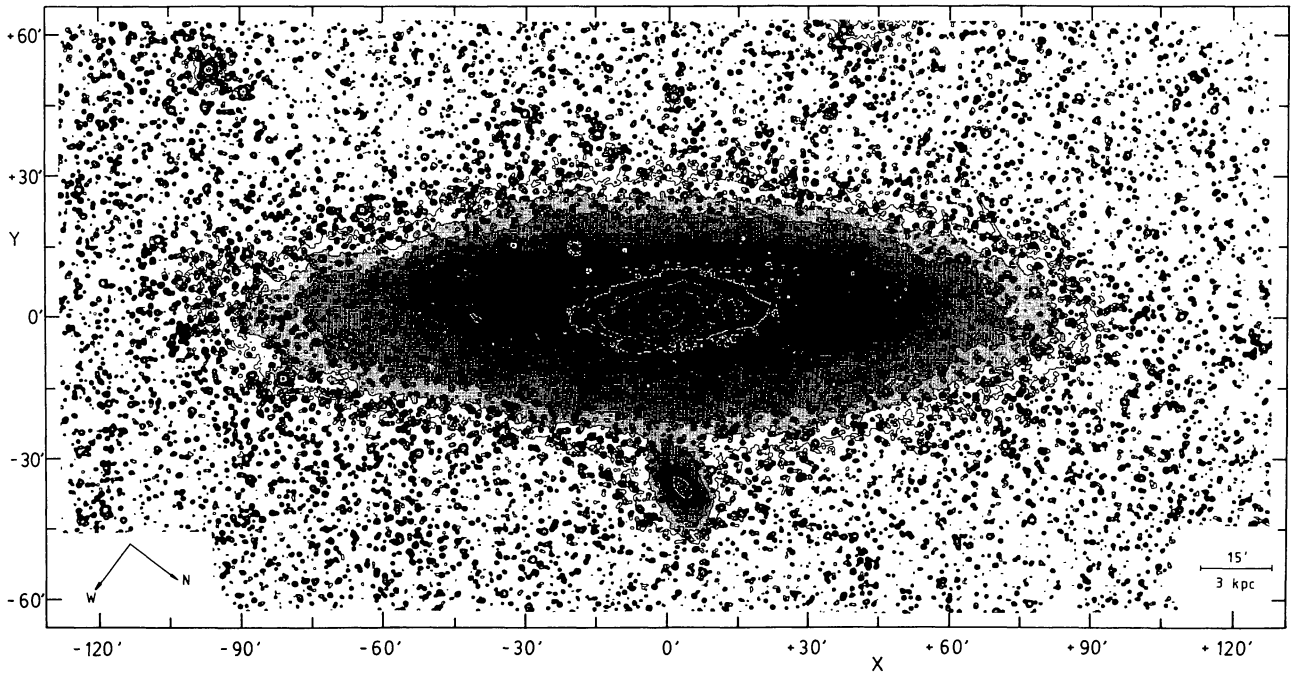

FIGURE 5. — (a) Light distribution of the Andromeda galaxy in the J (IIIaJ + GG385) band, smoothed to a 40″ beam, before removal of foreground stars. Contour levels (in mag arcsec^{-2}) : 19, 20, 21 and then in steps of 0.5 to 25.0.

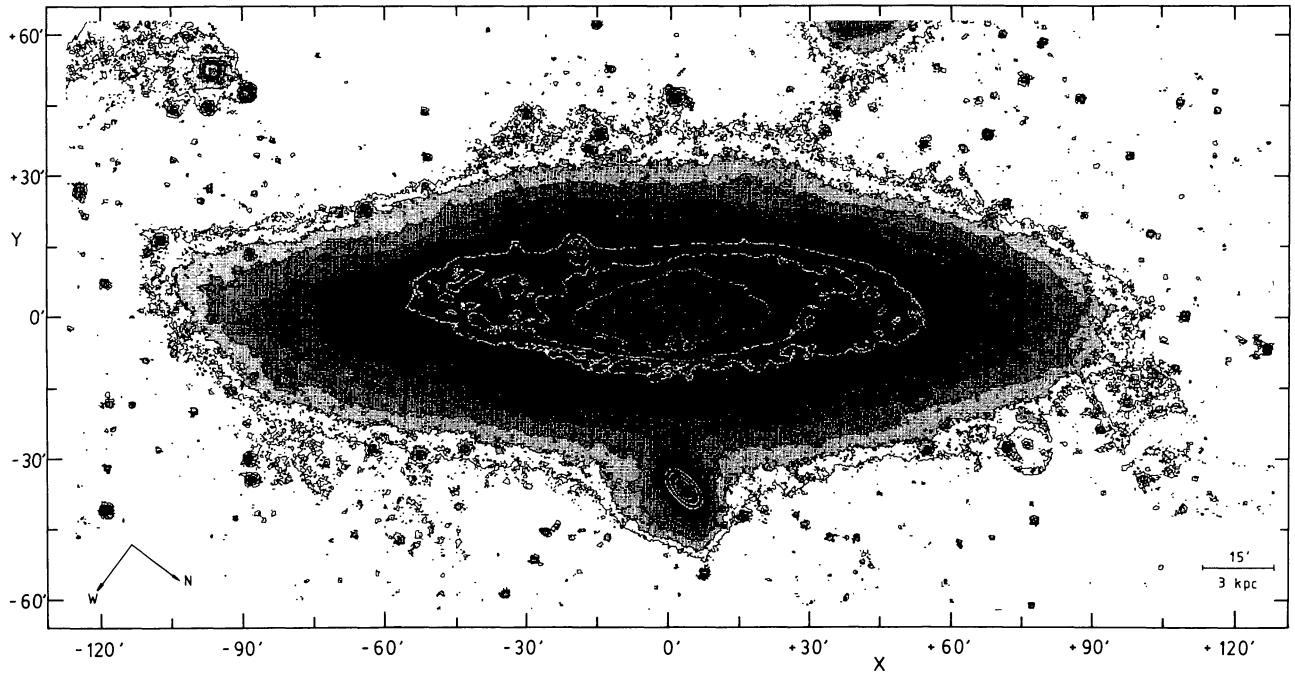

FIGURE 5. — (b) Light distribution as in figure 5(a), but after « rigorous star removal » (Sect. 3.5). The light of the galaxy can now be traced to much fainter levels. Note the twisting of the isophotes near NGC 205. A warping of the stellar disk is suggested by the change in position angle of the SW major axis near $X = -100'$. Only the brightest foreground stars cannot be removed completely. A ghost image of a star is visible near $X = +75'$, $Y = -27'$. The extension near NGC 205, at $X = -10'$, $Y = -37'$ may be due to the ghost image of the bulge of M31. The diffuse light near $X = +35'$, $Y = +60'$ is due to ν And, the brightest star in the field. The noise on this picture is lower than in figure 5(a), because the noise peaks are clipped in the automatic star removal routine. Contour levels (in mag arcsec^{-2}) : 19, 20, 21 and then in steps of 0.5 to 26.0.

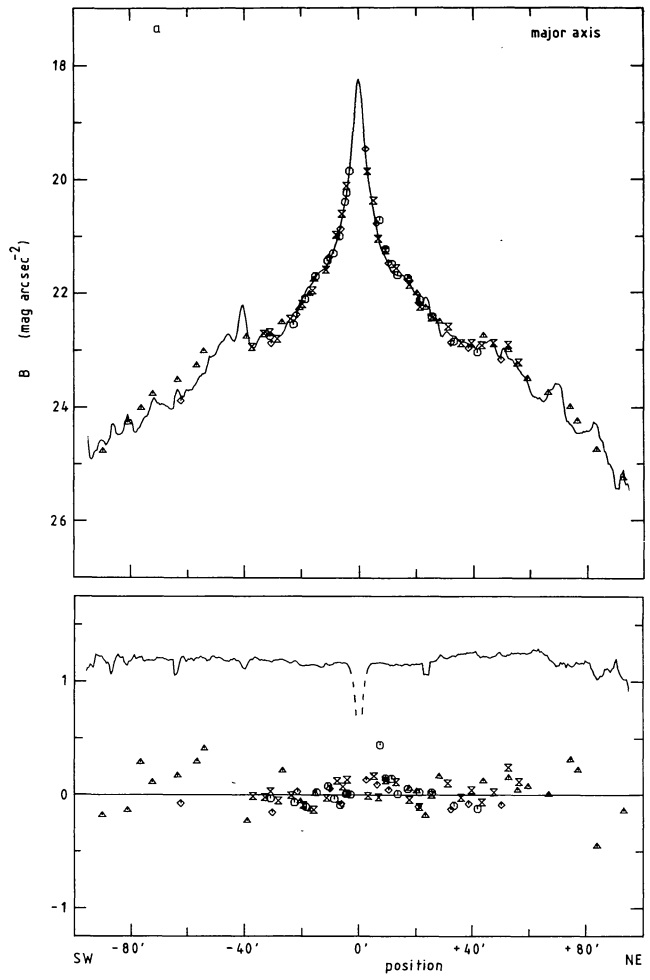

FIGURE 6. — (a) Major axis profile. The IIIaJ photometry is not correct in the centre where even the short *J* exposure was still saturated. References : *triangles* - de Vaucouleurs (1958) ; *circles* - Lyngå (1959) ; *diamonds* - Burgess (1976) ; *hourglasses* - Fricke (1954).

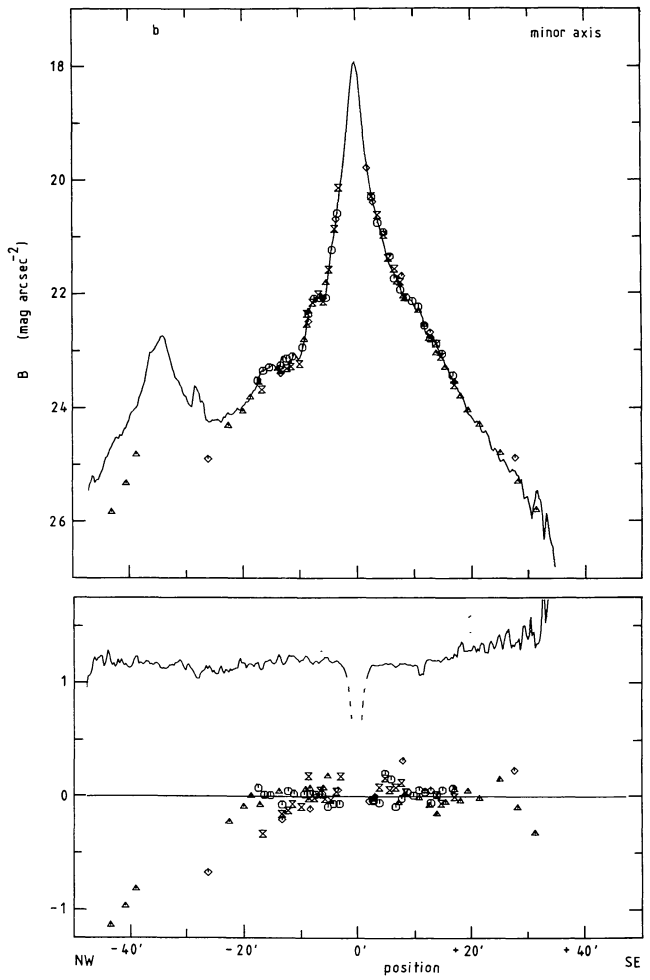

FIGURE 6. — (b) Minor axis profile, 60″ aperture. The discrepancy West of NGC 205 (around – 40′) may be caused by the ghost image of the bulge of M31 on our plates. References as in figure 6(a).

FIGURES 6. — Comparison between our *B* and IIIaJ photometry and published data. The brightest foreground stars were subtracted from our data. The top half of the figure shows the *B* profile determined from simulated aperture photometry through a 120″ aperture (full drawn line), and the published data (symbols). The colors of the published data and the vertical offset that was applied to give an average difference of zero can be found in table II. The lower half of the figure shows the difference between our photometry and the published data (symbols), and the difference between our *B* and IIIaJ photometry (*B-J* ; full drawn line). The zero point of the IIIaJ photometry is shifted arbitrarily. Note that most of the scatter between published data and our data is not due to errors in the photometry, but to small positional differences, color differences, different aperture sizes, foreground stars, etc.

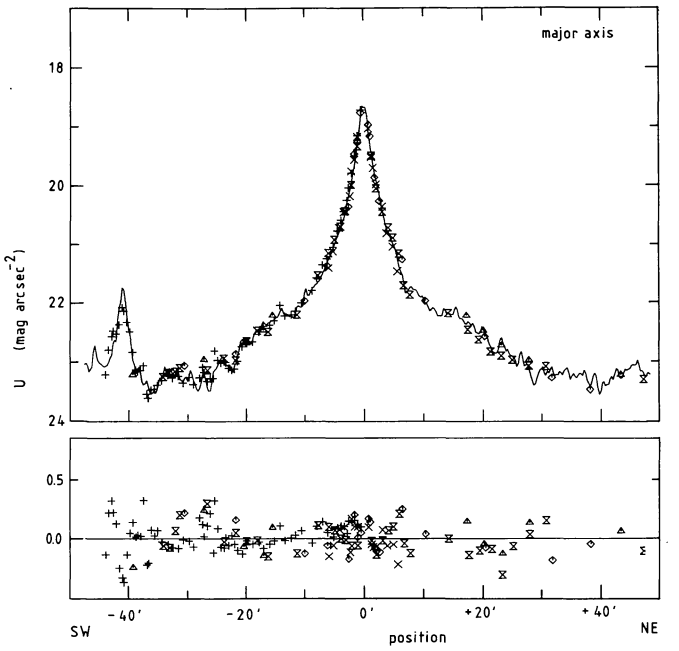

FIGURE 7. — Comparison between our *U* photometry (30″ aperture) and published data for the inner part of the major axis. See figure 6 for details. References : *triangles* - de Vaucouleurs (1958) ; *diamonds* - Burgess (1976) ; *hourglasses* - Fricke (1954) ; *crosses* - Sharov and Lyutyj (1980) ; *plusses* - Hoessel and Melnick (1980 ; positions rescaled as explained in text).

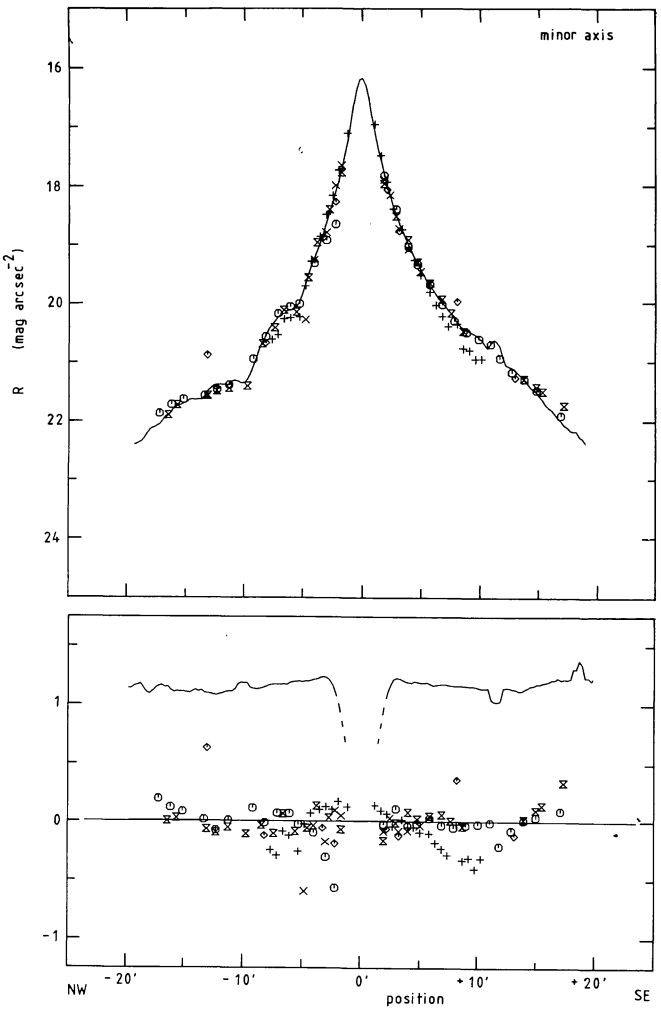

FIGURE 8. — Comparison between our *R* photometry (60″ aperture) and published data for the minor axis of M31. See figure 6 for details. The curve in the lower half of the figure shows the difference between our *R* and IIIaF photometry. The zero point of the F photometry is arbitrary. The *F* plates are saturated in the centre. There is a serious discrepancy with the data from Hoessel and Melnick *(plusses)*, we suspect as a result of a positional error in their data. References : *diamonds* - Burgess (1976) ; *circles* - Lyngå (1959) ; *hourglasses* - Fricke (1954) ; *crosses* - Sharov and Lyutyj (1980) ; *plusses* - Hoessel and Melnick (1980).

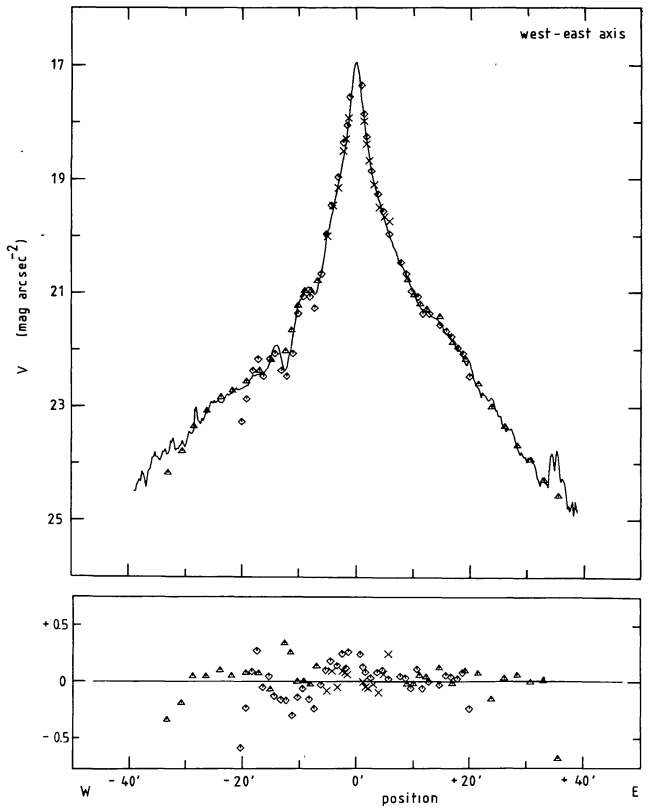

FIGURE 9. — Comparison of our *V* photometry (60″ aperture) with published data for the West-East axis of M31. See figure 6 for details. References : *triangles* - de Vaucouleurs (1958) ; *diamonds* - Burgess (1976) ; *crosses* - Sharov and Lyutyj (1980).

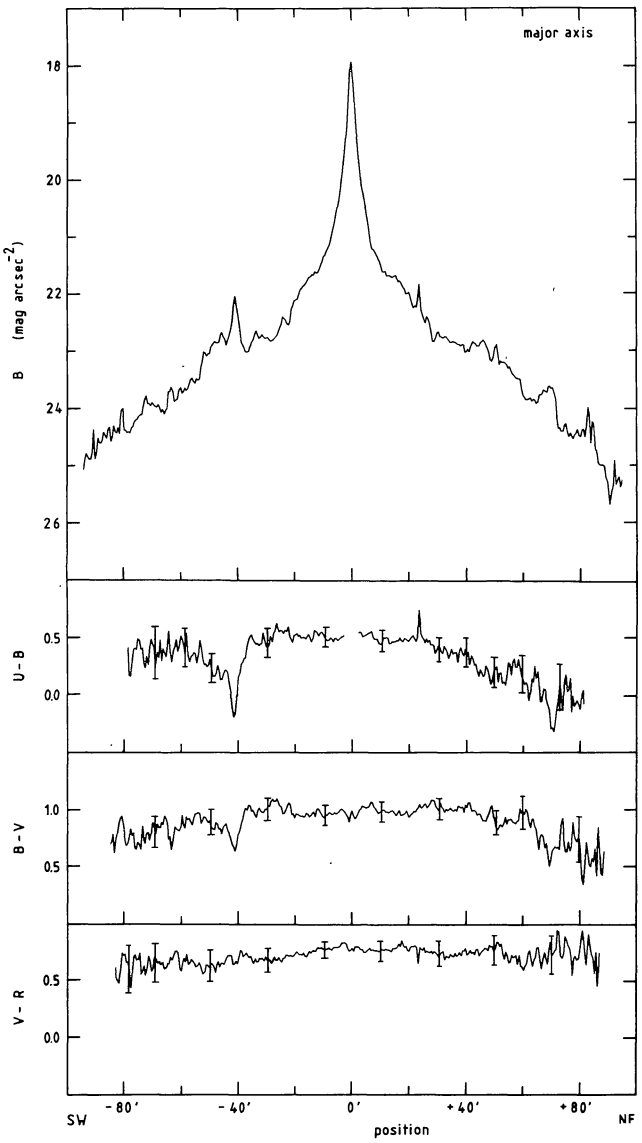

FIGURE 10. — (a) Major axis. The bright blue peak near − 40′ is the OB association NGC 206. On the opposite side spiral-arm crossings can also be seen. The sharp peak near + 22′ is a foreground star that was apparently missed by the automatic star removal procedure on the *B* map.

FIGURES 10. — Intensity and color profiles for the principal axes of M31 derived after removal of the brightest stars from our data, through a 60″ aperture (Sect. 3.5). Representative error bars are shown in the major axis profile. These are based on the estimated uncertainties listed in table III. They indicate the possible errors in the colors over large distances. The small-scale variations in the color profiles are real ; they reflect high resolution structure in the intensity maps, such as dust lanes, OB associations, weak foreground stars, etc.

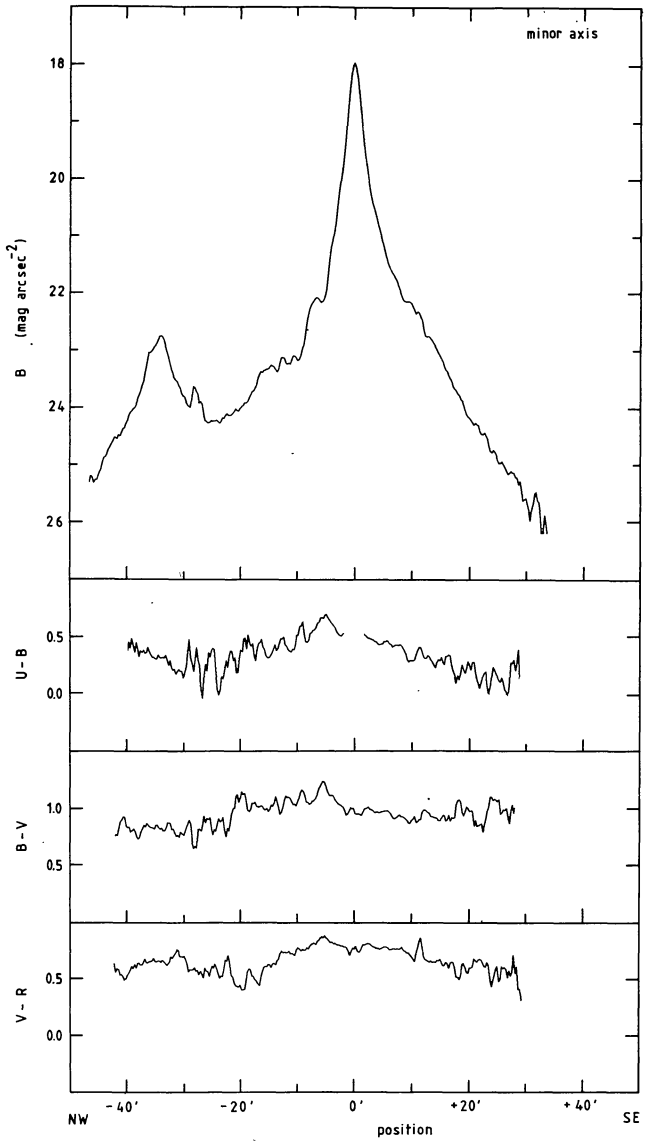

FIGURE 10. — (b) Minor axis. Dust lanes on the West side can be recognized as a reddening of the colors around − 6′ and − 10′. The hump to the left is due to the elliptical companion NGC 205.

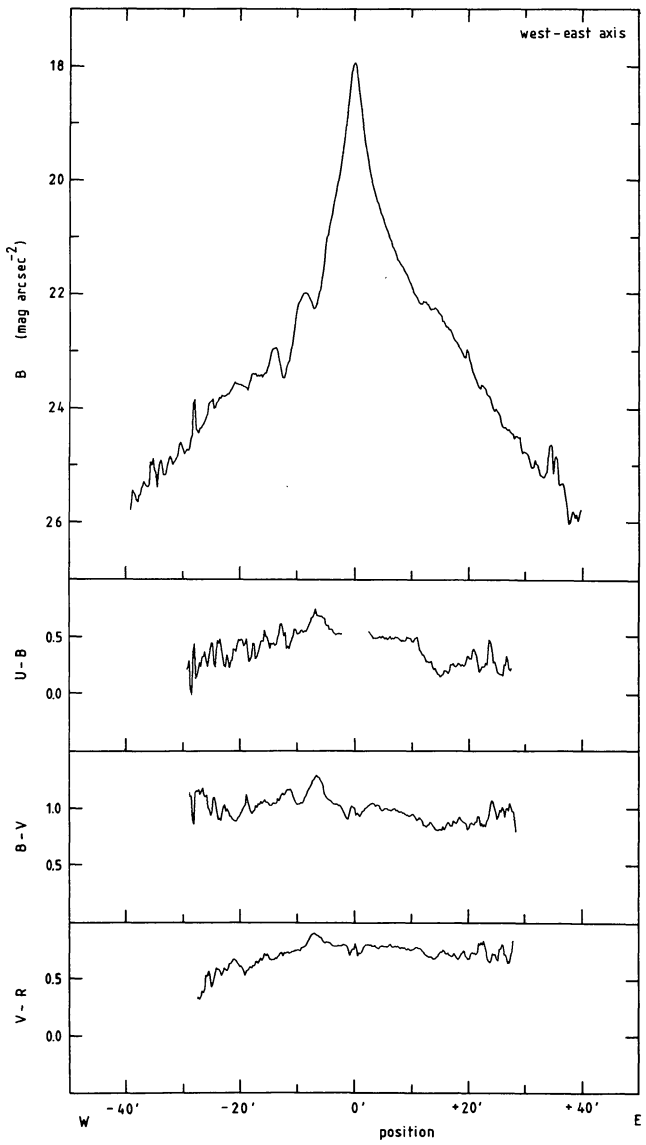

FIGURE 10. — (c) West-East axis. Red features on the West side correspond to strong dust lanes. The crossing of the bright NE arm around 10 kpc from the nucleus is apparent in the *U-B* and *B-V* profiles near + 10′ to + 20′.

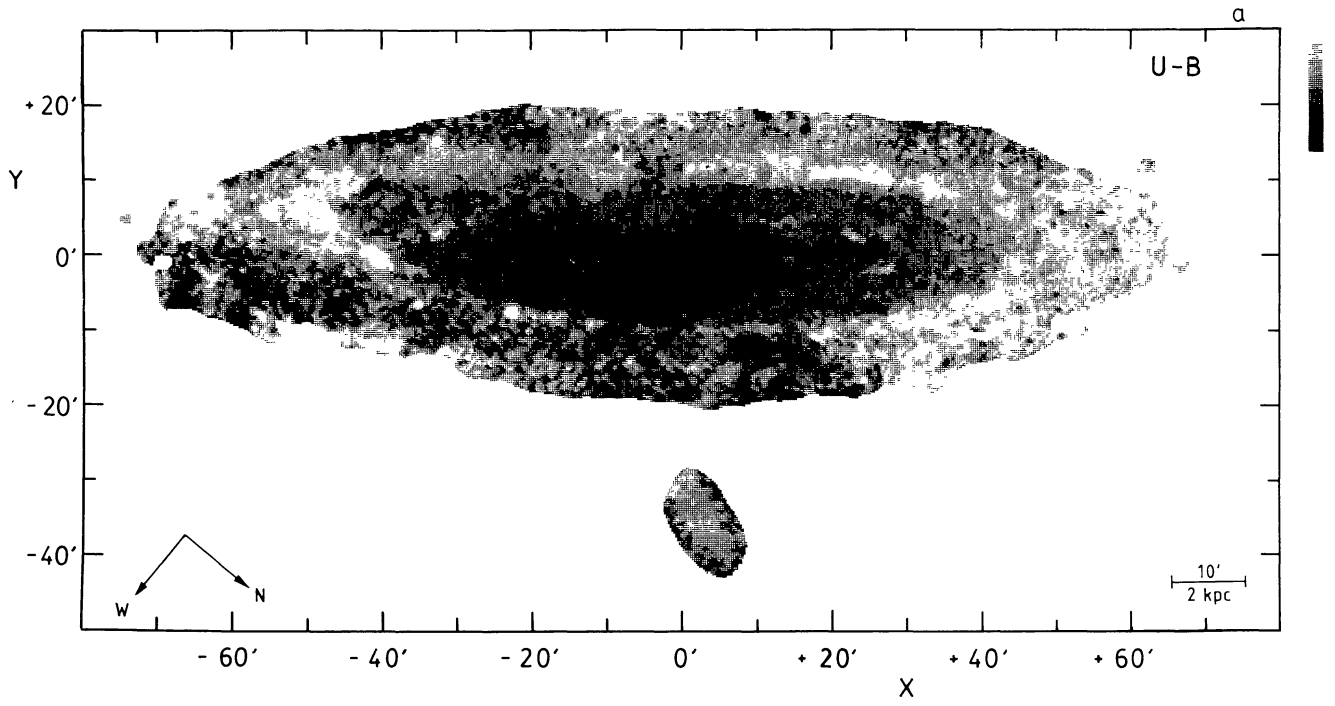

FIGURE 11. — (a) *U-B*, gray levels (from light to dark) : < 0.05, 0.05-0.15, 0.15-0.25, 0.25-0.35, 0.35-0.45, 0.45-0.55, 0.55-0.65, > 0.65.

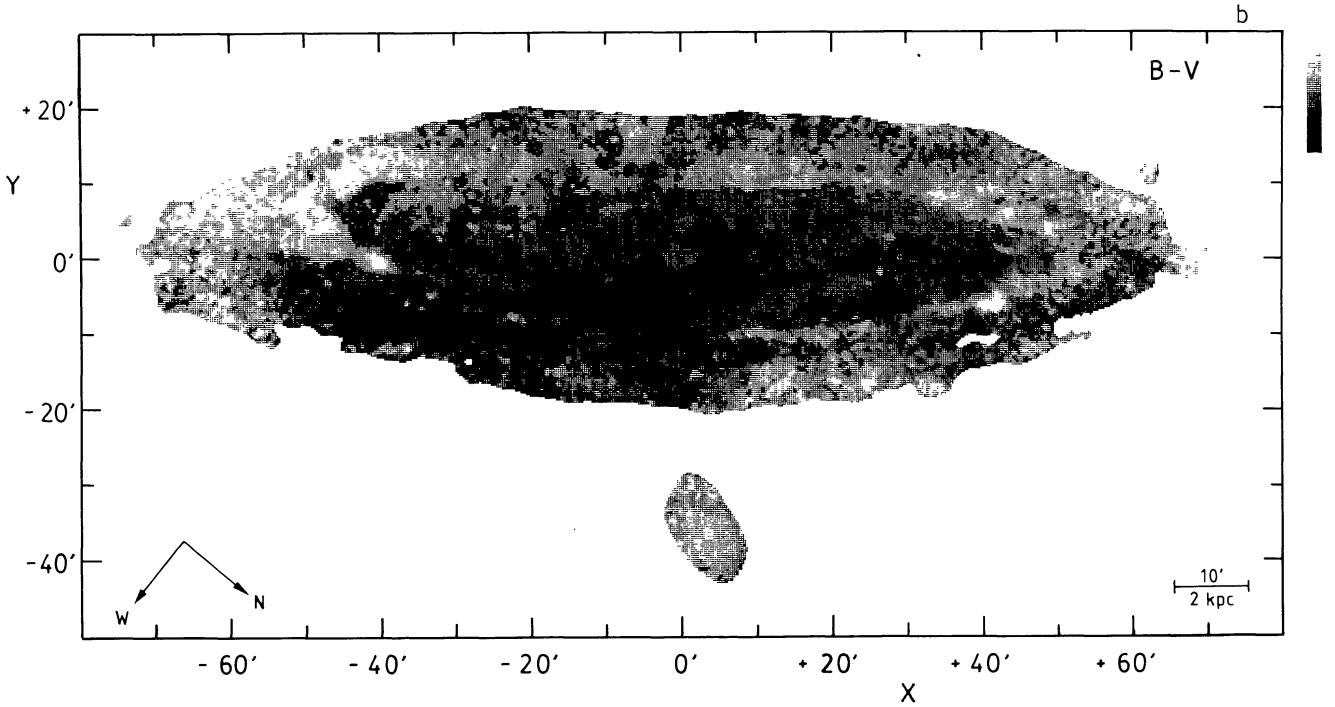

FIGURE 11. — (b) *B-V*, gray levels (from light to dark) : < 0.66, 0.66-0.74, 0.74-0.82, 0.82-0.90, 0.90-0.98, 0.98-1.06, 1.06-1.14, > 1.14.

FIGURES 11. — Color maps of M31 at 40″ resolution, obtained from the data after « light » star removal. Only regions for which the surface brightness in *B* is higher than 24.0 mag arcsec^{-2} are shown ; at lower light levels the colors quickly become unreliable.

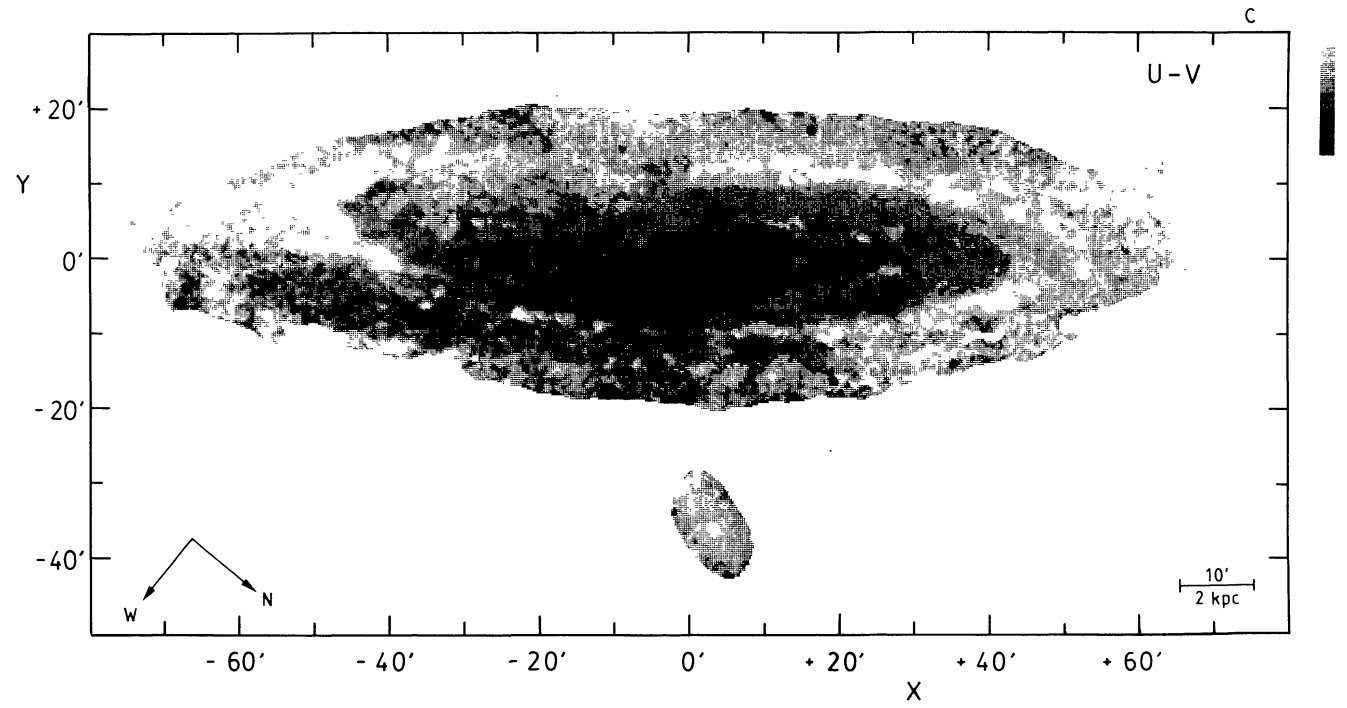

FIGURE 11. — (c) *U-V*, gray levels (from light to dark): < 0.90, 0.90-1.03, 1.03-1.16, 1.16-1.29, 1.29-1.42, 1.42-1.55, 1.55-1.68, > 1.68.

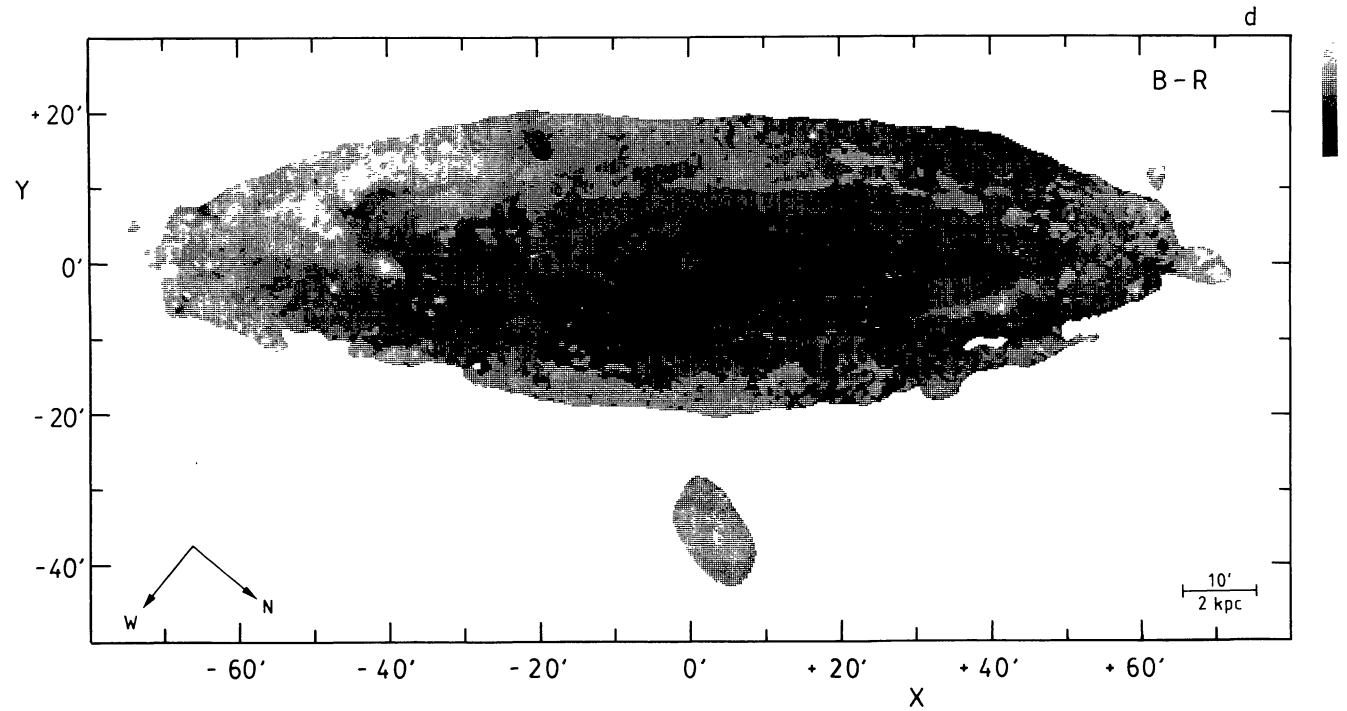

FIGURE 11. — (d) *B-R*, gray levels (from light to dark): < 1.24, 1.24-1.36, 1.36-1.48, 1.48-1.60, 1.60-1.72, 1.72-1.84, 1.84-1.96, > 1.96.

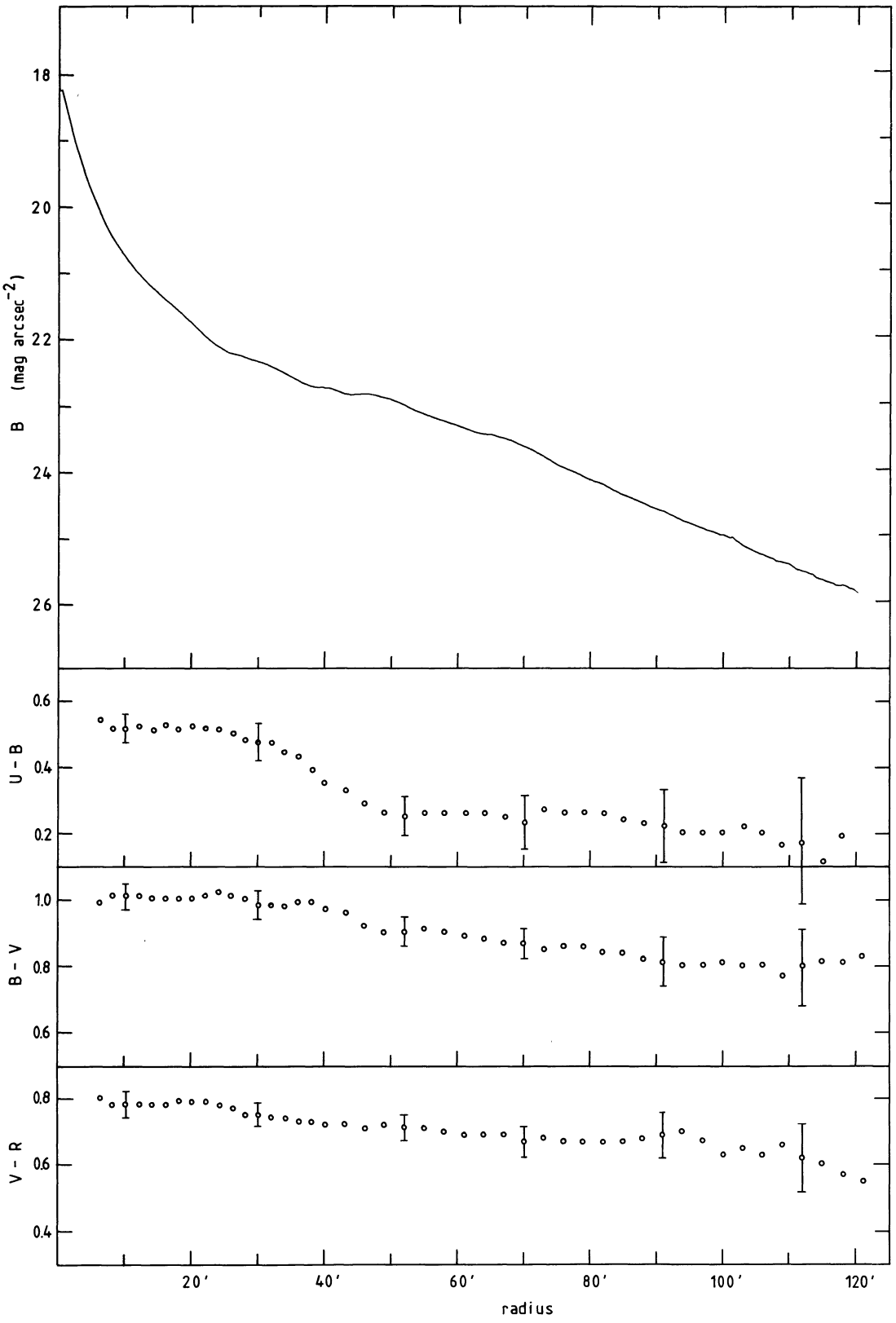

FIGURE 12. — The global light and color profiles of M31 obtained from the data by averaging the intensity distributions in ellipses centred on the nucleus of the galaxy. Foreground stars were removed from the data beforehand. The uncertainties were estimated from comparisons of the global profiles derived from different plates in the same color band.